Artifact analysis on B-splines, box-splines and other surfaces defined by quadrilateral polyhedra

U. H. Augsdörfer[a], N. A. Dodgson[a], M. A. Sabin[b]

[a]*Computer Laboratory, University of Cambridge, 15 J. J. Thomson Ave, Cambridge CB3 OFD, England*
[b]*Numerical Geometry Ltd., 19 John Amner Close, Ely, Cambridge CB6 1DT, England*

Abstract

When using NURBS or subdivision surfaces as a design tool in engineering applications, designers face certain challenges. One of these is the presence of artifacts. An artifact is a feature of the surface that cannot be avoided by movement of control points by the designer. This implies that the surface contains spatial frequencies greater than one cycle per two control points. These are seen as ripples in the surface and are found in NURBS and subdivision surfaces and potentially in all surfaces specified in terms of polyhedrons of control points.

Ideally, this difference between designer intent and what emerges as a surface should be eliminated. The first step to achieving this is by understanding and quantifying the artifact observed in the surface.

We present methods for analysing the magnitude of artifacts in a surface defined by a quadrilateral control mesh. We use the subdivision process as a tool for analysis. Our results provide a measure of surface artifacts with respect to initial control point sampling for all B-Splines, quadrilateral box-spline surfaces and regular regions of subdivision surfaces. We use four subdivision schemes as working examples: the three box-spline subdivision schemes, Catmull-Clark (cubic B-spline), 4-3, 4-8; and Kobbelt's interpolating scheme.

Key words: artifact, B-splines, box-splines, subdivision

1. Introduction

The design of NURBS or subdivision surfaces involves two steps: First, the designer translates his mental image of a shape into the definition of a polyhedron. Then, the B-spline function or subdivision scheme determines the surface corresponding to that polyhedron.

We can divide the surface into components with spatial frequencies below the Nyquist limit and those with spatial frequencies above. The designer can control the first group of components by moving control points, and so we assume that this group gives in some sense the desired curve. However, the designer cannot control the second group and these are what we call artifacts.

Email addresses: `Ursula.Augsdorfer@cl.cam.ac.uk` (U. H. Augsdörfer), `Neil.Dodgson@cl.cam.ac.uk` (N. A. Dodgson), `malcolm@geometry.demon.co.uk` (M. A. Sabin)

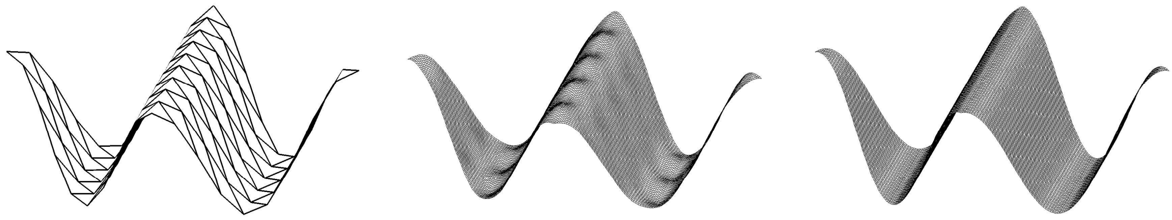

Figure 1: *Left: A quadrilateral control mesh with a surface feature not aligned with grid lines but aligned diagonally. Centre: the control mesh is refined using a subdivision scheme with* $(1 + z)$ *factors along the grid directions only. Lateral artifacts are clearly visible. Right: the control mesh has been subdivided using a scheme with* $(1 + z)$ *factors along the grid direction and diagonal directions.*

To be able to make an appropriate choice of which scheme and how many control vertices to use we need to provide the designer with the information of exactly how artifacts vary with the scheme and sampling density.

In our work we show how artifacts vary with respect to the sampling density and how large they are at any given sampling density. We explain how subdivision can be employed as a tool for the analysis of artifacts which appear in the surface and which are not controllable by the designer. The mechanism described provides a uniform framework for analysing artifacts present in regular regions of subdivision surfaces as well as in bivariate B-splines and quadrilateral box-splines.

Subdivision is an algorithmic technique to generate smooth surfaces as the limit of a sequence of successively refined polyhedra. Each subdivision step can be viewed as a multi stage process involving a refinement or sampling stage followed by one or more smoothing stages. We show that artifact components are inevitably introduced in the sampling stage. The signal and the artifact components are then both smoothed out in subsequent smoothing stages. In the limit this process will result in a B-spline surface the degree of which depends on the number of smoothing stages in each subdivision step. When handling schemes not based on B-splines we may encounter, alongside simple sampling and smoothing stages, a kernel from which no more smoothing stages can be extracted. By analysing the effect of the smoothing stages and the kernel on both the input signal and the artifact components, we are able to make a statement about their magnitude after one subdivision step.

The magnitude of the signal and artifact component after one subdivision step will be reduced with further subdivision steps. We show how our framework of artifact analysis can be extended to determine the magnitude of signal and artifact components in the limit curve or surface.

The analysis demonstrated here enables the designer to make a judgement on the necessary density of control points to use to be within certain required error margins, and also supplies a framework for the design of new algorithms, i.e. the analysis provides us with a tool to design schemes for which the error/artifact is zero at a certain sampling frequency.

2. Types of artifacts

Sabin et al. (2005) analysed artifacts in the univariate case. In the bivariate case, Sabin and

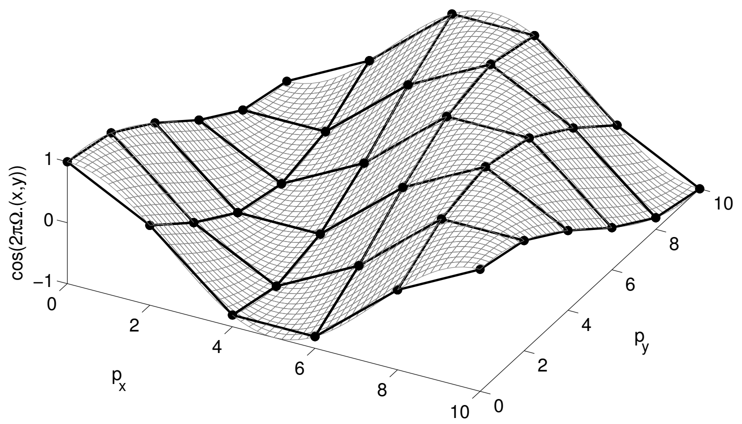

Figure 2: *The input mesh (black) has been sampled from a sinusoidal surface (grey) of the form* $\cos(2\pi\Omega.(x, y))$*. In this example* $\Omega = [0.1, 0.2]$*. Points indicate the vertices of the control polyhedron.*

Barthe (2003) identified two types of artifacts in the regular regions of subdivision surfaces: longitudinal artifacts, which are analogous to the univariate artifact and have the same direction as an intended feature of the surface; and lateral artifacts, which have a different direction across the surface to the intended feature. The other two artifacts identified by Sabin and Barthe (2003) relate to the effects of extraordinary points in subdivision surfaces. We have studied these in (Augsdörfer et al., 2006) and do not repeat that material here.

2.1. Longitudinal artifacts

Longitudinal artifacts are associated with the approximating error introduced in the sampling process. Although these artifacts are generally mild in effect, slightly altering the shape of the profiles involved, they are present for any surface with a uniform, stationary subdivision construction (which includes B-splines). These artifacts can be reduced, but not eliminated, either by choosing a subdivision scheme based on a B-spline of higher degree or by increasing the density of control points. The first has the disadvantage of giving looser control (larger support); for these schemes altering the position of one point will have an effect on a wider range of surrounding points which may not be the designer's intention. The latter has the disadvantage that more data has to be provided and that subsequent modifications require the movement of more control points.

2.2. Lateral artifacts

Lateral surface artifacts are more readily visible and occur when an extrusion runs in a direction not aligned with the underlying grid. An example of a lateral surface artifact is shown in Figure 1.

For binary subdivision schemes, directions for which these artifacts do not occur have been identified by Peters and Shiue (2004) as those in which the symbol of the mask of the scheme has a $(1 + z)$ factor. Details on why this is so are given in Section 3. There are four directions in which the $(1 + z)$ factors may be extracted from the mask. In this paper we use the arrow notation $\uparrow\!\!\!\rightarrow$ for axis aligned $(1 + z)$ factors and $\nwarrow\!\!\nearrow$ for diagonal $(1 + z)$ factors of a scheme. This notation was first introduced by Dodgson et al. (2009).

In the surface artifact analysis both longitudinal and lateral artifacts result from one mechanism and our analysis considers them together. In Section 5 we discuss a way of extracting information about lateral artifacts alone from results obtained from the joint analysis.

3. Method of analysis

In order to analyse the behaviour we sample the original data, $A_J,\ J \in \mathbb{Z}^2$, from a 2D sine wave of frequency Ω, measured in units of complete cycles per original vertex. An actual data set can be regarded as the sum of such components by Fourier theory, and, because the system updating from one step to the next is linear, we can separate the initial data into components of different spatial frequency, and look at the response of each component as a function of frequency. The effect on the total is the sum of the effects on the separate spatial frequency components.

The analysis for surfaces follows closely the univariate analysis, discussed by Sabin et al. (2005), except that abscissa positions and spatial frequencies are now bivariate objects.

We use the letter $J = (x, y),\ x,\ y \in \mathbb{Z}$, to denote the grid points before refinement and $P = (p_x, p_y),\ p_x,\ p_y \in \mathbb{Z}$ for the grid points after sampling. The bivariate spatial frequency, Ω, is represented as a vector with two components, ω_x and ω_y, where ω_x measures the number of complete cycles per point along the x axis and ω_y measures the number of complete cycles per point along the y axis. A short vector Ω implies long distances between crests and thus a low sampling frequency.

The input mesh is given by $A_J = e^{i\pi\Omega\cdot 2J} = T^{\Omega\cdot 2J}$, where $T = e^{i\pi}$. An example of an input mesh is shown in Figure 2.

3.1. Artifacts after one subdivision step

A subdivision step creates a new finer mesh by constructing new vertices as linear combinations of old ones. The coefficients of the linear combinations can be depicted as a *mask*, which documents the coefficients by which a given old vertex influences the surrounding new ones. Many properties of the limit subdivision surface can be determined by analysing the mask of a subdivision scheme. A useful tool for analysis is the z-transform of a mask.

Sabin et al. (2005) showed how a subdivision matrix can be factorised into a sampling matrix and a filter matrix. The filter matrix can be further factorised into a number of smoothing matrices and a kernel. The circulant factors in the smoothing matrices correspond to the $(1 + z)$ factors, referred to as smoothing factors, of the z-transform of the mask for a scheme (Dyn, 2002). The number of circulant smoothing matrices which can be extracted from the filter matrix is equivalent to the number of smoothing factors which can be extracted from the z-transform of the mask of a scheme. The kernel is what remains after all the smoothing factors have been extracted. For example the mask of the Catmull and Clark (1978) subdivision scheme for regular regions in the

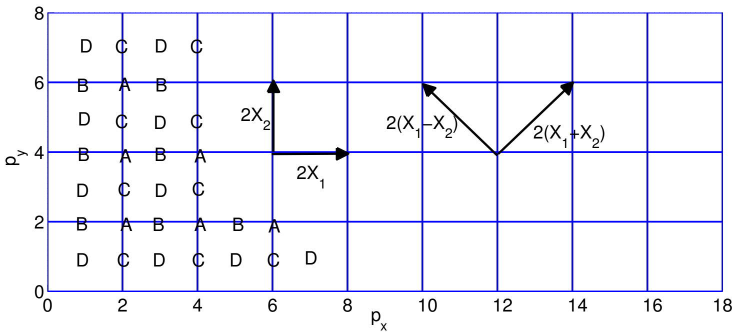

Figure 3: *Parameter space of a quadrilateral grid and the labelling used in Section 3. The mesh before sampling is shown in blue. The mesh after sampling is not shown.* X_1 *and* X_2 *are unit shifts in the newly sampled mesh.*

mesh can be resolved into four smoothing factors and a unit kernel such that

$$\frac{1}{64}\begin{bmatrix} 1 & 4 & 6 & 4 & 1 \\ 4 & 16 & 24 & 16 & 4 \\ 6 & 24 & 36 & 24 & 6 \\ 4 & 16 & 24 & 16 & 4 \\ 1 & 4 & 6 & 4 & 1 \end{bmatrix} = 4\left(\frac{1}{4}\begin{bmatrix} 1 & 1 \\ 1 & 1 \end{bmatrix} * \frac{1}{4}\begin{bmatrix} 1 & 1 \\ 1 & 1 \end{bmatrix} * \frac{1}{4}\begin{bmatrix} 1 & 1 \\ 1 & 1 \end{bmatrix} * \frac{1}{4}\begin{bmatrix} 1 & 1 \\ 1 & 1 \end{bmatrix} * [1]\right)$$

which corresponds to a z-transform of

$$4\left(\frac{1+z_1}{2}\right)^4\left(\frac{1+z_2}{2}\right)^4 \qquad \text{or, in arrow notation,} \qquad \begin{array}{l} \uparrow \\ \uparrow \\ \uparrow \\ \uparrow\!\!\!\rightarrow \rightarrow \rightarrow \rightarrow \end{array}$$

We assume the validity of the partitioning of the subdivision process into first a sampling stage, with insertion of zero elements at all new positions, followed by a series of convolutions with smoothing factors of the mask as discussed by Sabin et al. (2005).

3.1.1. The effect of sampling

We use the symbols X_1 and X_2 to denote the unit shifts in the abscissa plane along the two grid directions of the sampled rectangular grid. Thus $X_1 + X_2$ and $X_1 - X_2$ become shifts in diagonal directions, see Figure 3.

In a binary scheme sampling multiplies the original values by 4 and inserts zero values on mid edges and mid faces, such that

$$\begin{aligned} S_{2J} &= 4A_J \\ S_{2J+X_1} &= 0 \\ S_{2J+X_2} &= 0 \\ S_{2J+(X_1+X_2)} &= 0 \end{aligned}$$

On a rectangular grid the sampling process may be viewed as a tensor product:

$$\begin{aligned} S_p &= T^{\Omega \cdot P}(1 + \cos(\pi X_1 \cdot P))\,(1 + \cos(\pi X_2 \cdot P)) \\ &= \quad T^{\Omega \cdot P} \\ &\quad + T^{\Omega \cdot P}(T^{X_1 \cdot P} + T^{-X_1 \cdot P})/2 \\ &\quad + T^{\Omega \cdot P}(T^{X_2 \cdot P} + T^{-X_2 \cdot P})/2 \\ &\quad + T^{\Omega \cdot P}(T^{(X_1+X_2) \cdot P} + T^{-(X_1+X_2) \cdot P})/4 \\ &\quad + T^{\Omega \cdot P}(T^{(X_1-X_2) \cdot P} + T^{-(X_1-X_2) \cdot P})/4. \end{aligned}$$

We thus have diagonal artifacts as well as those along the grid lines expected from the tensor product formulation. When we consider a signal which is neither oriented along nor perpendicular to the grid edges, the artifacts, which remain aligned relative to the grid, can no longer be described as purely longitudinal (along the features) or purely lateral (diagonal or across the surface features).

We can rewrite the above as

$$\begin{aligned} S_P &= \quad T^{\Omega \cdot P} \\ &\quad + T^{\Omega \cdot P}(T^{X_1 \cdot P} + T^{-X_1 \cdot P})/2 \\ &\quad + T^{\Omega \cdot P}(T^{X_2 \cdot P} + T^{-X_2 \cdot P})/2 \\ &\quad + T^{\Omega \cdot P}(T^{X_1 \cdot P} + T^{-X_1 \cdot P})(T^{X_2 \cdot P} + T^{-X_2 \cdot P})/4. \end{aligned}$$

Hence, the artifact terms in the two different diagonal directions are linked and we have only three independent artifact terms.

This shows that a binary sampling stage on a quadrilateral grid results in a surface which is made up of four components of shape given by

$$\begin{aligned} &a\, T^{\Omega \cdot P}, \\ &b\, T^{\Omega \cdot P}(T^{X_1 \cdot P} + T^{-X_1 \cdot P})/2, \\ &c\, T^{\Omega \cdot P}(T^{X_2 \cdot P} + T^{-X_2 \cdot P})/2, \\ &d\, T^{\Omega \cdot P}(T^{X_1 \cdot P} + T^{-X_1 \cdot P})(T^{X_2 \cdot P} + T^{-X_2 \cdot P})/4 \end{aligned}$$

where a, b, c and d are the respective magnitudes of the signal component, the artifact component in X_1 direction, the artifact component in X_2 direction and the artifact component in the diagonal directions D. After sampling, each component has unit amplitude, that is $a = b = c = d = 1$.

In the following section we determine how much the amplitudes of the four components alter in the subsequent smoothing stages.

3.1.2. The effect of smoothing

Each smoothing stage involves assigning the mean of its direct neighbouring points to a vertex. A smoothing stage along the gridlines in a quadrilateral mesh can be viewed as a tensor product of single smoothing stages, [1 1]/2, in the grid directions. It is given by

$$\frac{1}{2}\begin{bmatrix} 1 \\ 1 \end{bmatrix} \cdot \begin{bmatrix} 1 & 1 \end{bmatrix}/2 = \frac{1}{4}\begin{bmatrix} 1 & 1 \\ 1 & 1 \end{bmatrix}. \tag{1}$$

		V			
		0	X_1	X_2	D
H	X_1	$c^2_{X_1}$	$s^2_{X_1}$	$c^2_{X_1}$	$s^2_{X_1}$
	X_2	$c^2_{X_2}$	$c^2_{X_2}$	$s^2_{X_2}$	$s^2_{X_2}$
	$(X_1 + X_2)$	$c^2_{X_1+X_2}$	$s^2_{X_1+X_2}$	$s^2_{X_1+X_2}$	$c^2_{X_1+X_2}$
	$(X_1 - X_2)$	$c^2_{X_1-X_2}$	$s^2_{X_1-X_2}$	$s^2_{X_1-X_2}$	$c^2_{X_1-X_2}$

Table 1: *The table lists the effect of two smoothing steps* $[1\ 2\ 1]/4$ *in direction* H *on the four components of the sampled surface after one step of subdivision. The first column shows the amplification of the signal term,* $V = 0$*, and the latter three show the artifact term depending on direction of artifact component,* $V = X_1,\ X_2$*, or* D*, where* D *is the artifact component in both diagonal directions combined. Terms* $\cos(\pi\Omega{\cdot}H/2)$ *and* $\sin(\pi\Omega{\cdot}H/2)$ *are here and in all following tables written as* c_H *and* s_H *for simplicity.*

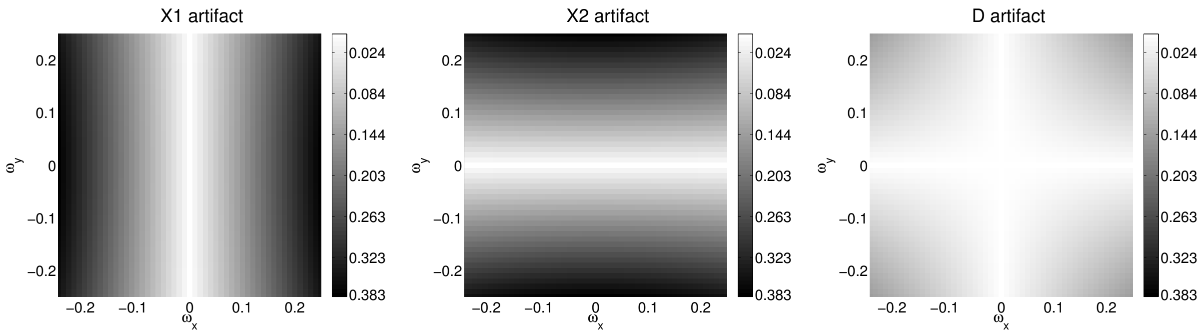

Figure 4: *The artifact amplitude depends on the sampling frequencies* ω_x *and* ω_y*, and is a sum of the amplitude of the three artifact components. Here, we show the amplitude of the three components, each plotted as functions of the sampling frequencies, after one subdivision step. These are 2D plots of the* Ω *parameter space. Note, that the diagonal artifact component is smaller than the components along the grid lines and only reaches a maximum of 0.15 for the sampling frequencies shown here. The subdivision step contains one single smoothing stage along each grid line direction of a quadrilateral mesh. In arrow notation this is* ↑→ *. The smoothing filter is:* $\frac{1}{4}\begin{bmatrix}1 & 1\\ 1 & 1\end{bmatrix}$.

In arrow notation this reads ↑→ . Additional smoothing diagonally to the gridlines requires convolution with the appropriate stencils

$$\frac{1}{4}\begin{bmatrix}1 & 1\\ 1 & 1\end{bmatrix} * \frac{1}{2}\begin{bmatrix}1 & 0\\ 0 & 1\end{bmatrix} * \frac{1}{2}\begin{bmatrix}0 & 1\\ 1 & 0\end{bmatrix} = \frac{1}{16}\begin{bmatrix} & 1 & 1 & \\ 1 & 2 & 2 & 1\\ 1 & 2 & 2 & 1\\ & 1 & 1 & \end{bmatrix}. \tag{2}$$

In arrow notation this stencil reads ↖↕↗→ , it has one smoothing stage in all four directions.

Taking the smoothing stages in pairs makes the analysis simpler (Sabin, 2002). We will demonstrate the effect of smoothing on each term by means of a double smoothing stage, $[1\ 2\ 1]/4$, in each direction. We can deal with smoothing in each direction independently.

Consider first the signal term, $T^{\Omega\cdot P}$. The convolution of this with $[1\ 2\ 1]/4$ in direction H,

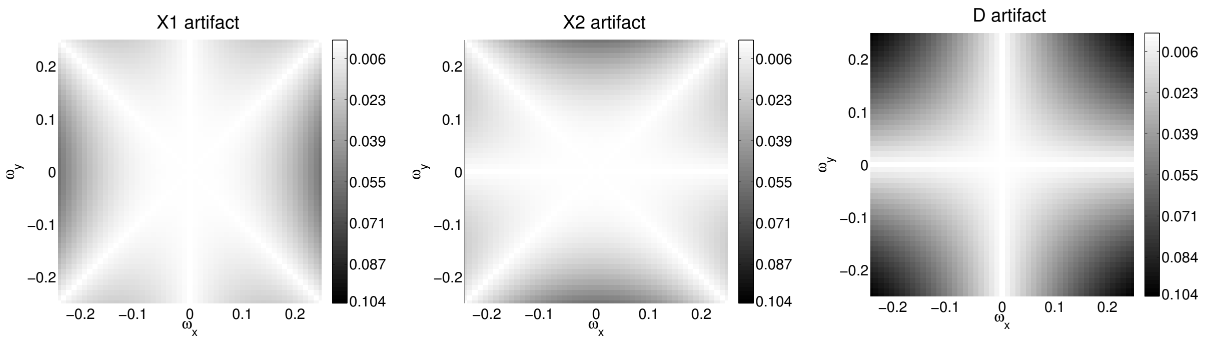

Figure 5: *The effect of a single subdivision step on the three artifact components is examined as in Figure 4. Note the difference in scaling compared to Figure 4. Here, the subdivision step contains one smoothing stage in all four directions of a quadrilateral mesh (along the grid lines and both diagonal directions). In arrow notation this is . As evident from these graphs, such smoothing will lead to considerably smaller artifacts for surface extrusions which run diagonal to the grid lines. The smoothing filter is:*

$$\frac{1}{16}\begin{bmatrix} & 1 & 1 & \\ 1 & 2 & 2 & 1 \\ 1 & 2 & 2 & 1 \\ & 1 & 1 & \end{bmatrix}$$

where H is X_1, X_2, $X_1 + X_2$ or $X_1 - X_2$, yields

$$\begin{aligned} &\left(T^{\Omega\cdot[P-H]} + 2T^{\Omega\cdot P} + T^{\Omega\cdot[P+H]}\right)/4 \\ &= T^{\Omega\cdot P}\cos^2(\pi\Omega\cdot H/2). \end{aligned} \tag{3}$$

If Ω and H lie in the same direction, their dot-product $(\Omega\cdot H)$ returns a non-zero scalar. However, if Ω is perpendicular to the smoothing direction H, their dot-product is zero $(\Omega\cdot H) = 0$ and no scaling occurs.

Next, consider the two artifact components along the grid-lines given by $(T^{V\cdot P} + T^{-V\cdot P})/2$, with V being a direction X_1 or X_2. The convolution with [1 2 1]/4 in direction H of this artifact component is

$$\begin{aligned} &\left(T^{\Omega\cdot[P-H]}\left(T^{V\cdot[P-H]} + T^{-V\cdot[P-H]}\right) + 2T^{\Omega\cdot P}\left(T^{V\cdot[P]} + T^{-V\cdot[P]}\right) + T^{\Omega\cdot[P+H]}\left(T^{V\cdot[P+H]} + T^{-V\cdot[P+H]}\right) \right)/8 \\ &= T^{\Omega\cdot P}\left(T^{-\Omega\cdot H}(T^{V\cdot P}T^{-V\cdot H} + T^{-V\cdot P}T^{V\cdot H}) + 2(T^{V\cdot P} + T^{-V\cdot P}) + T^{\Omega\cdot H}(T^{V\cdot P}T^{V\cdot H} + T^{-V\cdot P}T^{-V\cdot H}) \right)/8. \end{aligned}$$

There are only two cases to consider.

In one case, when the dot-product $(V\cdot H) = 0$, then $T^{V\cdot H} = T^{-V\cdot H} = 1$ and the above expression simplifies to

$$\begin{aligned} &T^{\Omega\cdot P}\left(T^{-\Omega\cdot H}(T^{V\cdot P} + T^{-V\cdot P}) + 2(T^{V\cdot P} + T^{-V\cdot P}) + T^{\Omega\cdot H}(T^{V\cdot P} + T^{-V\cdot P})\right)/8 \\ &= \left(T^{\Omega\cdot P}(T^{V\cdot P} + T^{-V\cdot P})/2\right)\cos^2(\pi\Omega\cdot H/2), \end{aligned} \tag{4}$$

so that the artifact component is multiplied by $\cos^2(\pi\Omega\cdot H/2)$. This only happens when the smoothing runs perpendicular to the artifact direction.

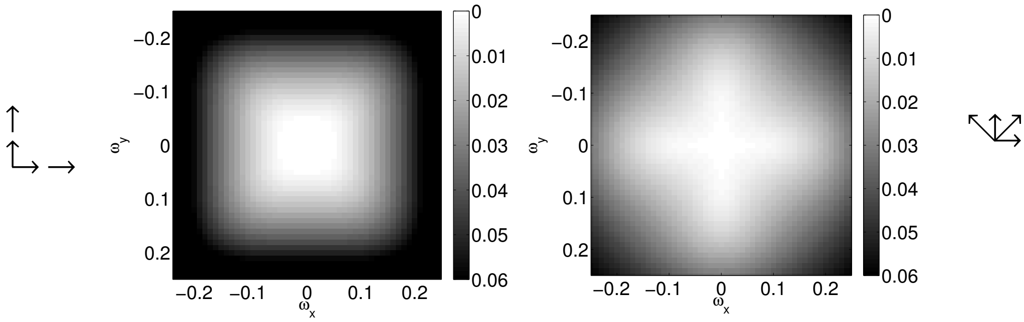

Figure 6: *The surface artifact energy is examined after one subdivision step containing four smoothing stages. Left: a scheme with two smoothing stages applied in each of the X_1 and X_2 direction, as for linear B-splines. Right: a scheme with one smoothing stage in X_1, X_2 and both diagonal directions. Adding diagonal smoothing to the scheme reduces the artifact contribution to the surface considerably for a large sampling range. The smoothing filters for left and right figures are, respectively* $\frac{1}{16}\begin{bmatrix} 1 & 2 & 1 \\ 2 & 4 & 1 \\ 1 & 2 & 1 \end{bmatrix}$ *and* $\frac{1}{16}\begin{bmatrix} & 1 & 1 & \\ 1 & 2 & 2 & 1 \\ 1 & 2 & 2 & 1 \\ & 1 & 1 & \end{bmatrix}$.

In the second case, when $(V{\cdot}H) = 1$, then $T^{V\cdot H} = T^{-V\cdot H} = -1$, a similar manipulation shows that the artifact component is multiplied by $\sin^2(\pi\Omega{\cdot}H/2)$. This occurs if the smoothing runs along the artifact component.

For artifact terms diagonal to the grid-lines smoothing has the effect:

$$
\begin{aligned}
= T^{\Omega\cdot P}\Big(& T^{-\Omega\cdot H}(T^{X_1\cdot P}T^{-X_1\cdot H} + T^{-X_1\cdot P}T^{X_1\cdot H})\,(T^{X_2\cdot P}T^{-X_2\cdot H} + T^{-X_2\cdot P}T^{X_2\cdot H}) \\
&+ 2(T^{X_1\cdot P} + T^{-X_1\cdot P})(T^{X_2\cdot P} + T^{-X_2\cdot P}) \\
&+ T^{\Omega\cdot H}(T^{X_1\cdot P}T^{X_1\cdot H} + T^{-X_1\cdot P}T^{-X_1\cdot H})\,(T^{X_2\cdot P}T^{X_2\cdot H} + T^{-X_2\cdot P}T^{-X_2\cdot H})\Big)/4.
\end{aligned}
$$

If the smoothing is along the grid lines, i.e. $H = X_1$ or $H = X_2$, the above expression simplifies to

$$\Big(T^{\Omega\cdot P}(T^{X_1\cdot P} + T^{-X_1\cdot P})(T^{X_2\cdot P} + T^{-X_2\cdot P})/4\Big)\ \sin^2(\pi\Omega{\cdot}H/2). \tag{5}$$

In the case when the smoothing is applied in either of the diagonal directions it simplifies to

$$\Big(T^{\Omega\cdot P}(T^{X_1\cdot P} + T^{-X_1\cdot P})(T^{X_2\cdot P} + T^{-X_2\cdot P})/4\Big)\ \cos^2(\pi\Omega{\cdot}H/2). \tag{6}$$

We tabulate these results in Table 1.

4. Visualising artifact magnitudes

We can visualise the effect smoothing has on each of the three artifact magnitudes as a function of sampling frequencies ω_x and ω_y in a 2D plot as in Figures 4 and 5.

Often the impact of each of the individual artifact components is not important, and a more useful indication of the quality of a scheme is obtained by computing their combined mean energy,

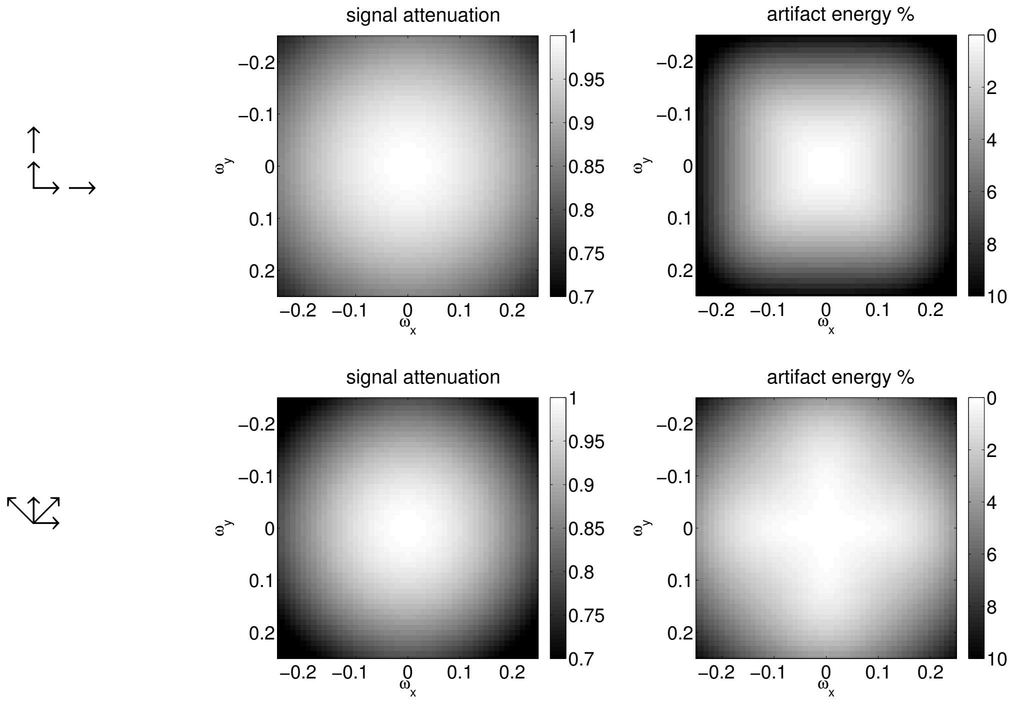

Figure 7: *The signal attenuation (left) and the energy of the artifact as a percentage of signal component (right) are examined after one subdivision step containing four smoothing stages. Top: a scheme with two smoothing stages in the X_1 and X_2 direction (top row) as for linear B-splines. Bottom: a scheme with one smoothing stage in X_1, X_2 and both diagonal directions (bottom row). The smoothing filters are as for Figure 6. These figures show that, although it increases the signal attenuation, including smoothing operations in the diagonal directions leads to an improved signal to artifact ratio.*

given by $\sqrt{(b^2 + c^2 + d^2)/3}$. Figure 6 compares the artifact energy after one subdivision step of two different subdivision schemes, each including four smoothing stages but in different directions.

It is also useful to show how the signal amplitude deteriorates for different sampling frequencies, as shown in Figure 7, on the left. The signal deterioration is a measure of how much of the initial information we are seeing at a given sampling rate. The grey scale visualisation, as used in Figures 4 – 7, readily reveals the quality of a scheme to the designer: the brighter the image, the more signal information has been retained or the smaller the magnitude of the artifact. Dark regions indicate big losses in signal information or a large artifact magnitude.

To get an indication of how visible the artifacts are in the surface, we should view them in relation to the remaining signal. If the artifacts are large in comparison to the attenuated signal they will be more visible in the smoothed surface, because a larger percentage of what we see is artifacts. It is therefore sensible to express the artifact as a percentage of the attenuated signal, $(100/a)\ \sqrt{b^2 + c^2 + d^2/3}$, see Figure 7, right.

The more smoothing stages are introduced the more the signal deteriorates and the more the artifact gets smoothed out. The choice of direction of smoothing also has an impact; Figure 6 demonstrates the dramatic effect of diagonal smoothing by comparing the artifact energy of two schemes with four smoothing stages. On the left smoothing has only been applied along the grid lines, as in B-splines, while on the right the scheme also includes diagonal smoothing stages.

Instead of plotting continuously varying grey scales, detail can be revealed more readily showing contour lines by delineating ranges of magnitudes, as in Figure 8. Diagonal smoothing on its own does not couple the vertex- and mid-face vertices with the mid-edge vertices. As can be clearly seen in the array of figures in Figure 8, if the scheme includes only diagonal smoothing, artifacts are present at low frequences because of this lack of coupling. On the other hand, adding diagonal smoothing to axis-aligned smoothing appears to be beneficial.

5. Magnitudes of lateral artifacts

As pointed out in the introduction, lateral artifacts in the limit surface are more visible than longitudinal artifacts. However, longitudinal and lateral artifacts are dealt with simultaneously in the bivariate analysis presented here and the magnitudes presented are compositions of both types of artifacts. To make an estimate about each type of artifact separately, we have to concentrate our attention on those parts of the artifact components where the extrusion of the data does not run along a smoothing direction. These type of extrusions, although both kinds of artifacts are present, will primarily be subjected to lateral artifacts.

To extract the lateral artifact information from the X_1 and X_2 artifact components, we determine the angle ϕ_1 between the extrusion of the data and one of the grid line directions, e.g. X_1.

$$\begin{aligned} \cos(\phi_1)\, \|\Omega\|\, \|X_1\| &= \Omega{\cdot}X_1 \\ \phi_1 &= \cos^{-1}\left(\frac{\Omega{\cdot}X_1}{\|\Omega\|}\right) \end{aligned}$$

To determine the lateral artifact magnitude in the X_1 artifact component we multiply the component by $\sin(\phi_1)$. The other angle to consider is ϕ_2 between the extrusion of the data and the grid line direction X_2, and we will multiply the X_2 artifact component by $\sin(\phi_2)$.

To extract the lateral artifact from the D artifact component we determine the angles ϕ_{d_1} and ϕ_{d_2}, between the extrusion of the data and the diagonal directions X_1+X_2 and X_1-X_2 respectively. Because the D artifact component contains the amount of artifact in both diagonal directions, we multiply the D artifact component by $\sin(\phi_{d_1})\sin(\phi_{d_2})$. This is a somewhat ad-hoc choice, justified only by the facts that it gives zeros matching the results of Peters and Shiue (2004) and that it provides a means of comparing different schemes without obvious bias.

We compare the energy of the lateral artifact in Figure 9. On the left, the lateral artifact for B-splines is shown, where no diagonal smoothing is present. On the right, smoothing in the diagonal direction has been added. The lateral artifact is considerably smaller for box-spline surfaces which include diagonal smoothing operations.

6. Artifacts in the limit

Table 1 lists artifact amplifications after a single subdivision step involving two smoothing stages. However, we have found that examining the response of the configuration after one subdivision step may overestimate the artifact present in the limit surface. In our analysis we aim to

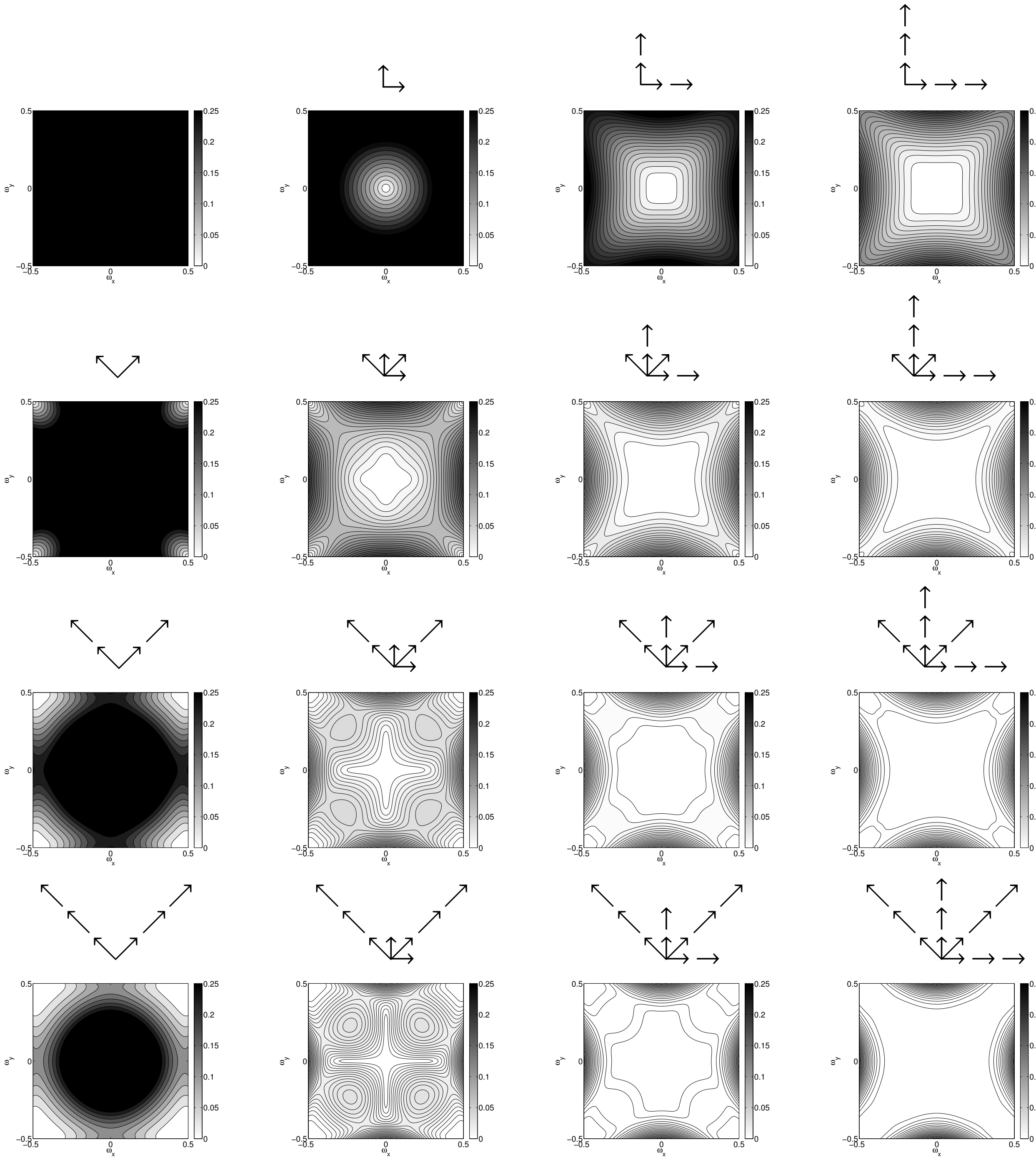

Figure 8: *The artifact energy after one subdivision step is shown as a function of a wide range of* $\Omega = [\omega_x, \omega_y]$. *The number of smoothing stages along the grid lines increase from left to right,* $((1+z_1)/2)^g((1+z_2)/2)^g$, $g \in [0, 1, 2, 3]$. *The number of diagonal smoothing stages increases from top to bottom,* $((1 + z_1 z_2)/2)^d\ ((1 + z_2/z_1)/2)^d$, $d \in [0, 1, 2, 3]$. *Schemes with equal numbers of smoothing stages therefore appear on upwardly sloped diagonals in the array of plots.*

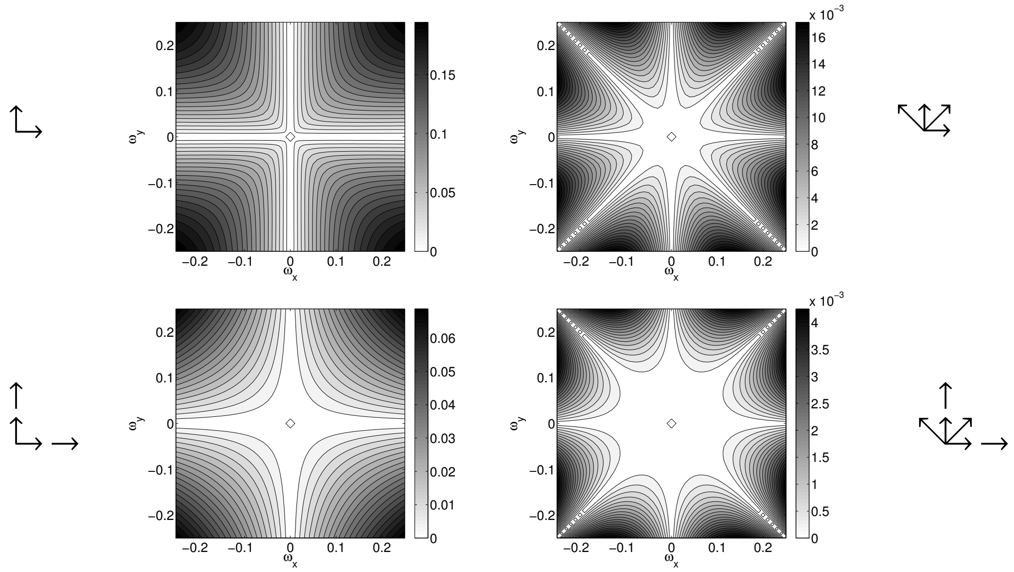

Figure 9: *The energy of the lateral artifact only is plotted as a function of $\Omega = [\omega_x, \omega_y]$ after one subdivision step. Figures on the left are obtained after a subdivision step including smoothing operations in the grid line directions only, while figures on the right are obtained after a subdivision step which also includes smoothing operations in both diagonal directions. Top: A single smoothing stage in the grid line directions. Bottom: Two smoothing stages in the grid line directions. Increasing the number of smoothing operations in the grid line directions in a subdivision step reduces the lateral artifact energy. But adding an extra smoothing operation in the diagonal operation reduces the lateral artifact energy considerably and thus reduce the appearance of ripples along the ridge of extruded features which are not aligned with the underlying mesh grid. The bottom left and top right schemes have the same number of arrows, but obviously different lateral artifact magnitudes. Note the difference in scales.*

determine the amplitude of the four shape components which make up the limit surface $L(P)$ such that

$$\begin{aligned} L(P) \quad = \quad & \alpha T^{\Omega \cdot P} \\ & + \beta T^{\Omega \cdot P} \cos(\pi X_1) \\ & + \gamma T^{\Omega \cdot P} \cos(\pi X_2) \\ & + \delta T^{\Omega \cdot P} \cos(\pi X_1) \cos(\pi X_2) \end{aligned}$$

where α, β, γ and δ are the magnitudes of signal and the three artifact components in the limit surface respectively.

In order to establish the effect of the subdivision process on the limit surface we have to identify points on the limit surface. Properties of the limit surface can be derived by a standard examination of the eigenstructure of the local subdivision matrix corresponding to the adopted subdivision scheme. The key to analysing the artifact of a subdivision surface in the limit is the row eigenvector corresponding to the dominant eigenvalue (Halstead et al., 1993). From this row eigenvector we can derive a limit stencil to determine points on the limit surface.

There are two ways of identifying the artifact in the limit: analysing one subdivision step and then the effect of the limit stencil or looking at the limit surface directly using limit stencils for vertex points, mid face points and mid edge points. To demonstrate this, we apply both methods to each of the examples discussed.

7. Examples

As a first example we look at the simplest of all quadrilateral subdivision schemes, the subdivision scheme based on the linear B-spline, before applying the same method of analysis to four more frequently used schemes each of which demonstrates particular features. The Catmull-Clark scheme (Catmull and Clark, 1978) is a widely used subdivision scheme based on the bicubic B-spline. The analysis of this scheme demonstrates how to determine the signal and artifacts magnitudes in the limit when not dealing with an interpolating scheme. The 4-3 box-spline scheme (Peters and Shiue, 2004) uses diagonal smoothing terms. It was found not to lead to lateral artifacts for extrusions diagonally to the gridlines. By analysing the effect of diagonal smoothing terms present in this scheme we demonstrate why this is the case. We then show that further improvements in the signal to artifact ratio can be achieved by adding further diagonal terms, using the 4-8 box-spline scheme (Velho and Zorin, 2001) as an example. Finally, we demonstrate how to handle the presence of a kernel in combination with smoothing terms using Kobbelt's interpolating scheme (Kobbelt, 1996) which is a subdivision scheme not based on a box-spline.

7.1. The bilinear B-spline

The mask of the subdivision scheme which leads to a bilinear B-spline surface in the limit is

$$\frac{1}{4}\begin{bmatrix} 1 & 2 & 1 \\ 2 & 4 & 2 \\ 1 & 2 & 1 \end{bmatrix} \tag{7}$$

The z-transform of the mask of this scheme can be factorised into

$$4\left(\frac{1+z_1}{2}\right)^2\left(\frac{1+z_2}{2}\right)^2 \qquad \text{or} \qquad \begin{array}{ll} \uparrow & \\ \Lsh\!\!\rightarrow & \rightarrow \end{array} \tag{8}$$

Hence, the bilinear B-spline has one [1 2 1]/4 factor in each grid direction and no diagonal smoothing. We can determine the signal and artifact magnitudes by multiplying together the appropriate number of factors from Table 1.

Because the scheme is interpolating, points of the initial control polyhedron lie on the limit surface. The results for the signal and artifact amplitude in the limit surface are listed in Table 2. In Figure 10 we show the signal deterioration, the artifact energy as a percentage of the remaining signal and the magnitude of the lateral artifact as a function of sampling frequencies. The magnitude of the lateral artifact associated with the linear B-spline, shown in Figure 10, right, was already discussed in Section 5.

7.1.1. Looking at the limit surface directly

We can look at the limit surface directly using the limit stencils derived from the row eigenvector corresponding to the dominant eigenvalue. The attenuation of the signal is determined by fitting the best sinusoidal approximation to the limit surface. The amplification of one of the three artifact components in the three directions (X_1, X_2, and diagonal) is given by the difference between the sum of the artifact component and the signal and the two remaining artifact components.

$a = \alpha$	$c_{X_1}^2 c_{X_2}^2$
$b = \beta$	$s_{X_1}^2 c_{X_2}^2$
$c = \gamma$	$c_{X_1}^2 s_{X_2}^2$
$d = \delta$	$s_{X_1}^2 s_{X_2}^2$

Table 2: *The magnitude of the signal term, α, and the artifact terms in the bilinear B-spline surface, where β, γ and δ are X_1, X_2 and diagonal direction artifact components respectively. Because the subdivision scheme based on the bilinear B-spline is interpolating the control polyhedron the amplification terms after one step are the same as in the limit surface.*

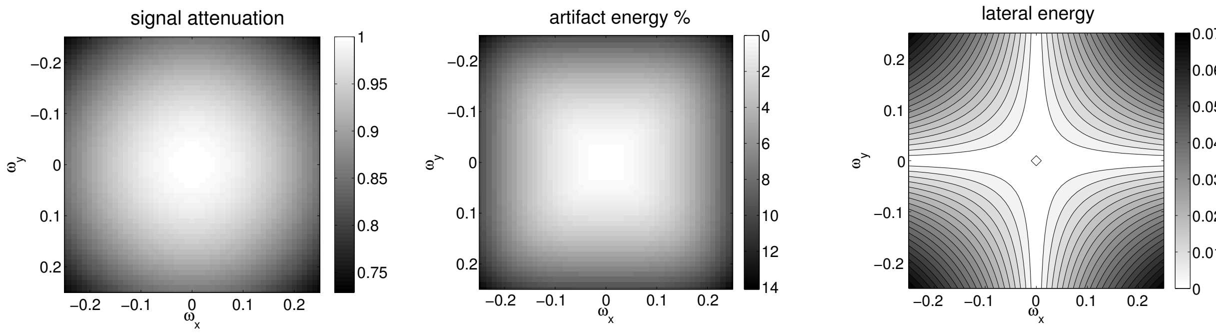

Figure 10: *Results for the linear B-spline are shown as a function of sampling frequency. Left: the signal magnitude. Centre: the artifact energy as a percentage of the attenuated signal. Right: the lateral artifact.*

Because this is an interpolating scheme, we can read off four limit stencils directly from the mask (7):

$$[4]/4\ ,\quad \begin{bmatrix} 1 & 1 \\ 1 & 1 \end{bmatrix}/4\ ,\quad \begin{bmatrix} 2 \\ 2 \end{bmatrix}/4\ ,\quad \text{and} \ \begin{bmatrix} 2 & 2 \end{bmatrix}/4.$$

namely a vertex limit stencil, the mid face limit stencil and the two mid edge limit stencils.

When convolving the vertex limit stencil with the signal, we just get the signal itself. Convolving the mid edge limit stencil with the signal we get

$$\left(2T^{\Omega\cdot 2(J-X_1/2)} + 2T^{\Omega\cdot 2(J+X_1/2)}\right)/4 = T^{\Omega\cdot 2J}\cos(\pi\Omega\cdot X_1)$$

The other edge limit stencil gives the equivalent result in the other direction $T^{\Omega\cdot 2J}\cos(\pi\Omega\cdot X_2)$.

Convolving the mid face limit stencil with the signal $T^{\Omega\cdot 2J}$ we get the limit surface component which is running diagonal to the grid-lines.

$$\begin{aligned}&\left(T^{\Omega\cdot 2(J-(X_1+X_2)/2)} + T^{\Omega\cdot 2(J+(X_1+X_2)/2)} + T^{\Omega\cdot 2(J-(X_1-X_2)/2)} + T^{\Omega\cdot 2(J+(X_1-X_2)/2)}\right)/4\\ &= T^{\Omega\cdot 2J}\cos(\pi\Omega\cdot X_1)\cos(\pi\Omega\cdot X_2)\end{aligned}$$

The sets of points obtained from these four stencils describe each a different sinusoidal surface, namely: $o\ T^{\Omega\cdot 2J}$, $p\ T^{\Omega\cdot 2J}$, $q\ T^{\Omega\cdot 2J}$ and $r\ T^{\Omega\cdot 2J}$, where $o = 1$, $p = \cos(\pi\Omega\cdot X_1)$, $q = \cos(\pi\Omega\cdot X_2)$ and $r = \cos(\pi\Omega\cdot X_1)\cos(\pi\Omega\cdot X_2)$. Any limit surface configuration can be expressed as the sum of these four components.

The best sinusoidal approximation to the limit surface, $\alpha T^{\Omega \cdot 2J}$, is thus given by the mean of these four components:

$$\begin{aligned} \alpha\, T^{\Omega \cdot 2J} &= T^{\Omega \cdot 2J}(o + p + q + r)/4 \\ &= \cos^2(\pi\Omega \cdot X_1/2)\cos^2(\pi\Omega \cdot X_2/2)\; T^{\Omega \cdot 2J} \end{aligned} \tag{9}$$

For example, if $\Omega = (w_x, 0)$, and the surface features vary in the x direction only, then $\alpha = \cos^2(\pi w_x/2)$ and we do not get any attenuation in the diagonal or X_2 direction.

The three artifact components of the limit surface the X_1, X_2 and the diagonal direction respectively, can be described as

$$\begin{aligned} \beta\, T^{\Omega \cdot 2J} &= T^{\Omega \cdot 2J}((o + q) - (r + p))/4 \\ &= T^{\Omega \cdot 2J}\left(1 - \cos(\pi\Omega \cdot X_1)\right)\left(1 + \cos(\pi\Omega \cdot X_2)\right)/4 \\ &= \sin^2(\pi\Omega \cdot X_1/2)\cos^2(\pi\Omega \cdot X_2/2)\; T^{\Omega \cdot 2J} \end{aligned} \tag{10}$$

$$\begin{aligned} \gamma\, T^{\Omega \cdot 2J} &= T^{\Omega \cdot 2J}((o + p) - (r + q))/4 \\ &= T^{\Omega \cdot 2J}\left(1 + \cos(\pi\Omega \cdot X_1)\right)\left(1 - \cos(\pi\Omega \cdot X_2)\right)/4 \\ &= \cos^2(\pi\Omega \cdot X_1/2)\sin^2(\pi\Omega \cdot X_2/2)\; T^{\Omega \cdot 2J} \end{aligned} \tag{11}$$

$$\begin{aligned} \delta\, T^{\Omega \cdot 2J} &= T^{\Omega \cdot 2J}((o + r) - (p + q))/4 \\ &= T^{\Omega \cdot 2J}\left(1 - \cos(\pi\Omega \cdot X_1)\right)\left(1 - \cos(\pi\Omega \cdot X_2)\right)/4 \\ &= \sin^2(\pi\Omega \cdot X_1/2)\sin^2(\pi\Omega \cdot X_2/2)\; T^{\Omega \cdot 2J} \end{aligned} \tag{12}$$

These results for the artifact amplification in the various directions are equivalent to the results we established earlier for the bilinear B-spline (see Table 2).

After demonstrating our method for the analysis of artifacts in the limit surface of a quadrilateral mesh for this simple example, we now turn our attention to schemes which are more complex and more commonly used.

7.2. The bicubic B-spline

In regular regions the Catmull-Clark subdivision scheme [Catmull and Clark (1978)] is a cubic tensor product bivariate box spline subdivision scheme. The mask of the scheme is

$$\frac{1}{64}\begin{bmatrix} 1 & 4 & 6 & 4 & 1 \\ 4 & 16 & 24 & 16 & 4 \\ 6 & 24 & 36 & 24 & 6 \\ 4 & 16 & 24 & 16 & 4 \\ 1 & 4 & 6 & 4 & 1 \end{bmatrix}. \tag{13}$$

Its z-transform is

$$4\left(\frac{1 + z_1}{2}\right)^4\left(\frac{1 + z_2}{2}\right)^4 \qquad \text{or} \qquad \begin{array}{l} \uparrow \\ \uparrow \\ \uparrow \\ \llcorner\!\!\to \to \to \to \end{array} \tag{14}$$

a	$c_{X_1}^4 c_{X_2}^4$
b	$s_{X_1}^4 c_{X_2}^4$
c	$c_{X_1}^4 s_{X_2}^4$
d	$s_{X_1}^4 s_{X_2}^4$

Table 3: *The magnitude of signal, a, and artifact components b, c and d in the X_1, X_2, and diagonal direction respectively, after one step using Catmull-Clark subdivision.*

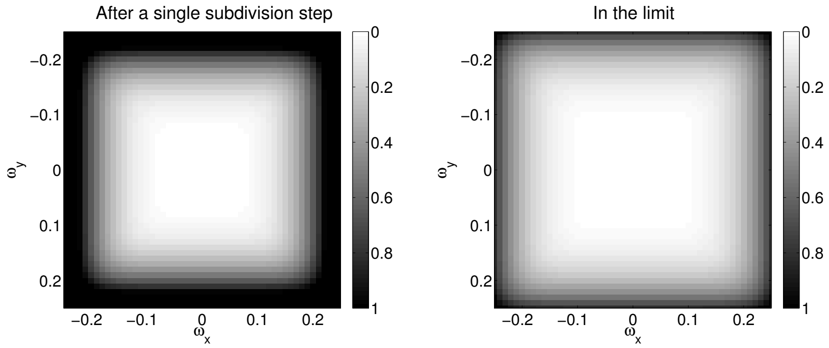

Figure 11: *The artifact energy as a percentage of the attenuated signal in the regular regions of the Catmull-Clark surface as a function of sampling frequency. Left: After one subdivision step using the Catmull-Clark algorithm. Right: The bicubic B-spline surface (regular regions of the Catmull-Clark limit surface).*

Thus, the bicubic box spline has two [1 2 1]/4 smoothing factors in each of the grid line directions. We can determine the artifact magnitude after one subdivision step by multiplying together the appropriate number of factors from Table 1. There is no diagonal smoothing.

The artifact energy after one subdivision step is larger than the artifact energy in the limit, see Figure 11. To determine the magnitudes of signal and artifact components of a bicubic B-spline surface we have to apply the corresponding limit stencils derived from the row eigenvectors corresponding to the dominant eigenvalue of the local subdivision matrix. In the regular regions the limit stencil for the Catmull-Clark scheme is

$$\frac{1}{36}\begin{bmatrix} 1 & 4 & 1 \\ 4 & 16 & 4 \\ 1 & 4 & 1 \end{bmatrix},$$

which has the z-transform

$$\left(\frac{1+4z_1+{z_1}^2}{6}\right)\left(\frac{1+4z_2+{z_2}^2}{6}\right).$$

We can rewrite the z-transform of the limit stencil in terms of smoothing factors. We divide the stencil written in z-transform notation by a power of z so that the central value corresponds to

α	$c^4_{X_1} c^4_{X_2}(1 + 2c^2_{X_1})(1 + 2c^2_{X_2})/9$
β	$s^4_{X_1} c^4_{X_2}(1 + 2s^2_{X_1})(1 + 2c^2_{X_2})/9$
γ	$c^4_{X_1} s^4_{X_2}(1 + 2c^2_{X_1})(1 + 2s^2_{X_2})/9$
δ	$s^4_{X_1} s^4_{X_2}(1 + 2s^2_{X_1})(1 + 2s^2_{X_2})/9$

Table 4: *The magnitude of signal, α, and artifact components β, γ and δ in the X_1, X_2, and diagonal direction respectively, in the bicubic B-spline surface (regular regions of the Catmull-Clark limit surface).*

z^0 and do likewise with the double smoothing operator, which becomes $(z^{-1} + 2z^0 + z^1)/4$. This leads to:

$$\left(\frac{z_1^{-1} + 4z_1^0 + z_1{}^1}{6}\right)\left(\frac{z_2^{-1} + 4z_2^0 + z_2{}^1}{6}\right) = \left(\frac{1}{3} + \frac{2}{3}\left(\frac{z_1^{-1} + 2z_1^0 + z_1^1}{4}\right)\right)\left(\frac{1}{3} + \frac{2}{3}\left(\frac{z_2^{-1} + 2z_2^0 + z_2^1}{4}\right)\right) \tag{15}$$

The attenuation of the signal and the amplification of the artifacts in the three directions are listed in Table 4.

7.2.1. Looking at the limit surface directly

Like for the bilinear B-spline, we can determine the signal attenuation and artifact amplification from the limit surface directly. By convolving the mask of the scheme with the limit stencil we can determine four limit stencils. The convolution of the mask with the limit stencil is

$$\left(\frac{1}{64}\begin{bmatrix} 1 & 4 & 6 & 4 & 1 \\ 4 & 16 & 24 & 16 & 4 \\ 6 & 24 & 36 & 24 & 6 \\ 4 & 16 & 24 & 16 & 4 \\ 1 & 4 & 6 & 4 & 1 \end{bmatrix}\right) * \left(\frac{1}{36}\begin{bmatrix} 1 & 4 & 1 \\ 4 & 16 & 4 \\ 1 & 4 & 1 \end{bmatrix}\right) = \frac{1}{2304}\begin{bmatrix} 1 & 8 & 23 & 32 & 23 & 8 & 1 \\ 8 & 64 & 184 & 256 & 184 & 64 & 8 \\ 23 & 184 & 529 & 736 & 529 & 184 & 23 \\ 32 & 256 & 736 & 1024 & 736 & 256 & 32 \\ 23 & 184 & 529 & 736 & 529 & 184 & 23 \\ 8 & 64 & 184 & 256 & 184 & 64 & 8 \\ 1 & 8 & 23 & 32 & 23 & 8 & 1 \end{bmatrix}.$$

We can simply read the four limit stencils off. The limit vertex stencil is the same as before the convolution with the mask:

$$\frac{1}{2304}\begin{bmatrix} 64 & 256 & 64 \\ 256 & 1024 & 256 \\ 64 & 256 & 64 \end{bmatrix} = \frac{1}{36}\begin{bmatrix} 1 & 4 & 1 \\ 4 & 16 & 4 \\ 1 & 4 & 1 \end{bmatrix}.$$

By convolving the stencil with the initial input we get

$$\begin{aligned} &\Big(T^{\Omega\cdot 2(J-X_1-X_2)} + 4T^{\Omega\cdot 2(J-X_2)} + T^{\Omega\cdot 2(J+X_1-X_2)} \\ &\quad + 4T^{\Omega\cdot 2(J-X_1)} + 16T^{\Omega\cdot 2J} + 4T^{\Omega\cdot 2(J+X_1)} \\ &\quad + T^{\Omega\cdot 2(J-X_1+X_2)} + 4T^{\Omega\cdot 2(J+X_2)} + T^{\Omega\cdot 2(J+X_1+X_2)}\Big)/36 \\ = \;& T^{\Omega\cdot 2J}\left(1 + 2\cos^2(\pi\Omega\cdot X_1)\right)\left(1 + 2\cos^2(\pi\Omega\cdot X_2)\right)/9. \end{aligned}$$

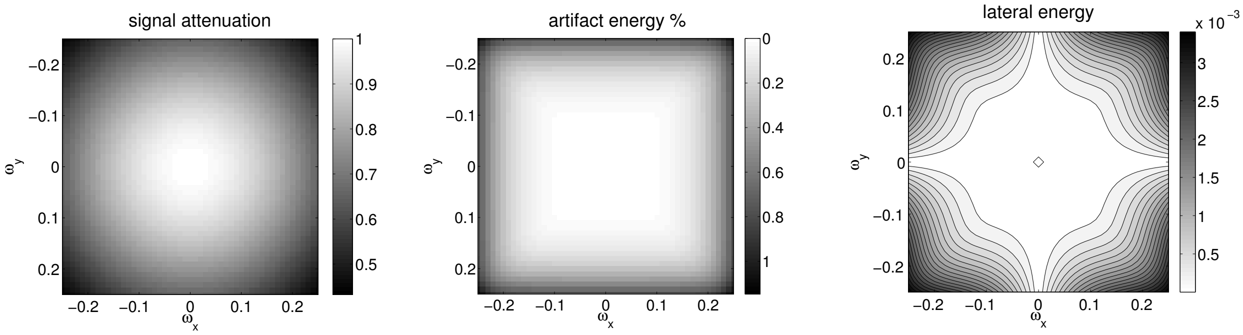

Figure 12: *Results for the bicubic B-spline (Catmull-Clark surface in the limit) as a function of sampling frequency. Left: the signal magnitude. Centre: the artifact energy as a percentage of the attenuated signal. Right: the lateral artifact.*

One limit mid edge stencil is

$$\frac{1}{2304}\begin{bmatrix} 8 & 32 & 8 \\ 184 & 736 & 184 \\ 184 & 736 & 184 \\ 8 & 32 & 8 \end{bmatrix} = \frac{1}{288}\begin{bmatrix} 1 & 4 & 1 \\ 23 & 92 & 23 \\ 23 & 92 & 23 \\ 1 & 4 & 1 \end{bmatrix}.$$

Its effect on the input signal is

$$T^{\Omega\cdot 2J}\left(1+2\cos^2(\pi\Omega\cdot X_1)\right)\left(\cos^3(\pi\Omega\cdot X_2)+5\cos(\pi\Omega\cdot X_2)\right)/18.$$

The second limit edge point stencil is like the above but rotated by 90 degrees. Its effect on the signal is

$$T^{\Omega\cdot 2J}\left(1+2\cos^2(\pi\Omega\cdot X_2)\right)\left(\cos^3(\pi\Omega\cdot X_1)+5\cos(\pi\Omega\cdot X_1)\right)/18.$$

The limit mid face stencil is

$$\frac{1}{2304}\begin{bmatrix} 1 & 23 & 23 & 1 \\ 23 & 529 & 529 & 23 \\ 23 & 529 & 529 & 23 \\ 1 & 23 & 23 & 1 \end{bmatrix}.$$

Its effect on the input signal $T^{\Omega\cdot 2J}$ is

$$T^{\Omega\cdot 2J}\left((\cos(3\pi\Omega\cdot X_1)+23\cos(\pi\Omega\cdot X_1))/24\right)\left((\cos(3\pi\Omega\cdot X_2)+23\cos(\pi\Omega\cdot X_2))/24\right).$$

And because $\cos(3\pi\Omega\cdot X) = 4\cos^3(\pi\Omega\cdot X) - 3\cos(\pi\Omega\cdot X)$ we have

$$T^{\Omega\cdot 2J}\left(\cos^3(\pi\Omega\cdot X_1)+5\cos(\pi\Omega\cdot X_1)\right)\left(\cos^3(\pi\Omega\cdot X_2)+5\cos(\pi\Omega\cdot X_2)\right)/36.$$

The limit points determined from the four limit stencils describe four different surfaces: $o\,T^{\Omega\cdot 2J}$, $p\,T^{\Omega\cdot 2J}$, $q\,T^{\Omega\cdot 2J}$ and $r\,T^{\Omega\cdot 2J}$, with

$$\begin{aligned}
o &= (1+2\cos^2(\pi\Omega\cdot X_1))(1+2\cos^2(\pi\Omega\cdot X_2))/9\\
p &= \left(1+2\cos^2(\pi\Omega\cdot X_1)\right)\left(\cos^3(\pi\Omega\cdot X_2)+5\cos(\pi\Omega\cdot X_2)\right)/18\\
q &= \left(1+2\cos^2(\pi\Omega\cdot X_2)\right)\left(\cos^3(\pi\Omega\cdot X_1)+5\cos(\pi\Omega\cdot X_1)\right)/18\\
r &= \left(\cos^3(\pi\Omega\cdot X_1)+5\cos(\pi\Omega\cdot X_1)\right)\left(\cos^3(\pi\Omega\cdot X_2)+5\cos(\pi\Omega\cdot X_2)\right)/36
\end{aligned}$$

The best sinusoidal approximation to the limit surface is given by $\alpha\,T^{\Omega\cdot 2J}$, and determined by equation (9) and leads to a signal magnitude, α, given by

$$\alpha = \cos^4(\pi\Omega\cdot X_1/2)\cos^4(\pi\Omega\cdot X_2/2)(1+2\cos^2(\pi\Omega\cdot X_1/2))(1+2\cos^2(\pi\Omega\cdot X_2/2))/9.$$

This result for the attenuation of the signal is the same as shown in Table 4, which was derived looking at the effect of sampling and smoothing stages and the effect of the limit stencil of the subdivision scheme.

The amplitudes β, γ and δ of the three artifact components of the limit surface in the X_1, X_2 and the diagonal direction respectively, are given by equations (10), (11) and (12) and lead equally to the same results for the amplification of the three artifact terms as shown in Table 4.

By comparing our results for the bicubic B-spline surface (Figure 12) to those for the bilinear B-spline surface (Figure 10) we find that by simply doubling the smoothing operations in the grid line directions we are able to improve the signal to artifact ratio considerably, by a factor of about 10.

Next, we will see that further improvements can be achieved by adding diagonal smoothing operations to each subdivision step.

7.3. The 4-3 box-spline

The 4-3 box-spline can model constant features without ripples both aligned with the quad grid and diagonal to it [Peters and Shiue (2004)]. We are able to demonstrate this quality by determining the magnitude of signal and artifact components as before.

The mask of the 4-3 scheme is

$$\frac{1}{16}\begin{bmatrix} & 1 & 2 & 1 & \\ 1 & 4 & 6 & 4 & 1\\ 2 & 6 & 8 & 6 & 2\\ 1 & 4 & 6 & 4 & 1\\ & 1 & 2 & 1 & \end{bmatrix}. \qquad (16)$$

The z-transform of this mask is given by

$$4\left(\frac{1+z_1}{2}\right)^2\left(\frac{1+z_2}{2}\right)^2\left(\frac{1+z_1z_2}{2}\right)\left(\frac{1+z_2/z_1}{2}\right) \qquad \text{or} \qquad \overset{\uparrow}{\nwarrow\!\!\nearrow}\!\!\rightarrow \qquad (17)$$

a	$c^2_{X_1}$	$c^2_{X_2}$	$c_{X_1+X_2}$	$c_{X_1-X_2}$
b	$s^2_{X_1}$	$c^2_{X_2}$	$s_{X_1+X_2}$	$s_{X_1-X_2}$
c	$c^2_{X_1}$	$s^2_{X_2}$	$s_{X_1+X_2}$	$s_{X_1-X_2}$
d	$s^2_{X_1}$	$s^2_{X_2}$	$c_{X_1+X_2}$	$c_{X_1-X_2}$

Table 5: *The magnitude of the signal and artifact terms after one subdivision step when using the 4-3 scheme, where b, c and d are the magnitudes of the artifacts in X_1, X_2 and diagonal direction respectively.*

It has two smoothing stages in each axial grid direction and one in each diagonal direction. By simply reading off the effect of the smoothing stages we get an artifact amplification after one subdivision step as listed in Table 5.

The limit stencil for this scheme is given by

$$\frac{1}{48}\begin{bmatrix} 1 & 6 & 1 \\ 6 & 20 & 6 \\ 1 & 6 & 1 \end{bmatrix}.$$

Its z-transform is

$$\frac{1}{48}\left(\left(1 + 6z_1 + {z_1}^2\right)\left(1 + 6z_2 + {z_2}^2\right) - 16\right).$$

As before we can rewrite the first part of the limit stencil in terms of smoothing factors as

$$[1\ 6\ 1] \quad = \quad (4 + 4([1\ 2\ 1]/4)).$$

Its effect on the input signal is therefore

$$\begin{aligned} &\frac{1}{48}\left(\left(4 + 4\cos^2(\pi\Omega{\cdot}X_1/2)\right)\left(4 + 4\cos^2(\pi\Omega{\cdot}X_2/2)\right) - 16\right) \\ &= \left(\left(1 + \cos^2(\pi\Omega{\cdot}X_1/2)\right)\left(1 + \cos^2(\pi\Omega{\cdot}X_2/2)\right) - 1\right)/3. \end{aligned}$$

The amplification factors are multiplied to those after a single step as shown in Table 6.

7.3.1. Looking at the limit surface directly

We can determine the same results by looking at the limit surface directly. By convolving the mask with the limit stencils we get four different set of points. While all of these points make up the limit surface, each set can be approximated by a different sinusoidal surface.

$$\left(\frac{1}{16}\begin{bmatrix} & 1 & 2 & 1 & \\ 1 & 4 & 6 & 4 & 1 \\ 2 & 6 & 8 & 6 & 2 \\ 1 & 4 & 6 & 4 & 1 \\ & 1 & 2 & 1 & \end{bmatrix}\right) * \left(\frac{1}{48}\begin{bmatrix} 1 & 6 & 1 \\ 6 & 20 & 6 \\ 1 & 6 & 1 \end{bmatrix}\right) = \frac{1}{768}\begin{bmatrix} 0 & 1 & 8 & 14 & 8 & 1 & 0 \\ 1 & 16 & 63 & 96 & 63 & 16 & 1 \\ 8 & 63 & 176 & 242 & 176 & 63 & 8 \\ 14 & 96 & 242 & 320 & 242 & 96 & 14 \\ 8 & 63 & 176 & 242 & 176 & 63 & 8 \\ 1 & 16 & 63 & 96 & 63 & 16 & 1 \\ 0 & 1 & 8 & 14 & 8 & 1 & 0 \end{bmatrix}.$$

α	$c_{X_1}^2\ c_{X_2}^2\ c_{X_1+X_2}\ c_{X_1-X_2}\left((1+c_{X_1}^2)(1+c_{X_2}^2)-1\right)/3$
β	$s_{X_1}^2\ c_{X_2}^2\ s_{X_1+X_2}\ s_{X_1-X_2}\left((1+s_{X_1}^2)(1+c_{X_2}^2)-1\right)/3$
γ	$c_{X_1}^2\ s_{X_2}^2\ s_{X_1+X_2}\ s_{X_1-X_2}\left((1+c_{X_1}^2)(1+s_{X_2}^2)-1\right)/3$
δ	$s_{X_1}^2\ s_{X_2}^2\ c_{X_1+X_2}\ c_{X_1-X_2}\left((1+s_{X_1}^2)(1+s_{X_2}^2)-1\right)/3$

Table 6: *The magnitude of the signal and artifact components in the 4-3 limit surface, where β, γ and δ are the X_1, X_2 and diagonal direction respectively.*

We can read off four limit stencils directly from this. The vertex limit stencil is the same as before

$$\frac{1}{768}\begin{bmatrix} 16 & 96 & 16 \\ 96 & 320 & 96 \\ 16 & 96 & 16 \end{bmatrix} = \frac{1}{48}\begin{bmatrix} 1 & 6 & 1 \\ 6 & 20 & 6 \\ 1 & 6 & 1 \end{bmatrix}.$$

Its effect on the input data can be analysed either as before, or by convolving it with the initial data:

$$\begin{aligned} &\Big(T^{\Omega\cdot 2(J-(X_1+X_2))} + 6T^{\Omega\cdot 2(J-X_2)} + T^{\Omega\cdot 2(J+(X_1-X_2))} \\ &+6T^{\Omega\cdot 2(J-X_1)} + 20T^{\Omega\cdot 2J} + 6T^{\Omega\cdot 2(J+X_1)} \\ &+T^{\Omega\cdot 2(J-(X_1-X_2))} + 6T^{\Omega\cdot 2(J+X_2)} + T^{\Omega\cdot 2(J+(X_1+X_2))}\Big)/48 \\ = \;& T^{\Omega\cdot 2J}\left((1+\cos^2(\pi\Omega\cdot X_1))(1+\cos^2(\pi\Omega\cdot X_2))-1\right)/3. \end{aligned}$$

The mid edge stencil is

$$\frac{1}{768}\begin{bmatrix} 1 & 14 & 1 \\ 63 & 242 & 63 \\ 63 & 242 & 63 \\ 1 & 14 & 1 \end{bmatrix}.$$

Its effect on the initial data is

$$\begin{aligned} &\Big(T^{\Omega\cdot 2(J-X_1-3X_2/2)} + 14T^{\Omega\cdot 2(J-3X_2/2)} + T^{\Omega\cdot 2(J+X_1-3X_2/2)} \\ &+ 63T^{\Omega\cdot 2(J-X_1-X_2/2)} + 242T^{\Omega\cdot 2(J-X_2/2)} + 63T^{\Omega\cdot 2(J+X_1-X_2/2)} \\ &+ 63T^{\Omega\cdot 2(J-X_1+X_2/2)} + 242T^{\Omega\cdot 2(J+X_2/2)} + 63T^{\Omega\cdot 2(J+X_1+X_2/2)} \\ &+ T^{\Omega\cdot 2(J-X_1+3X_2/2)} + 14T^{\Omega\cdot 2(J+3X_2/2)} + T^{\Omega\cdot 2(J+X_1+3X_2/2)}\Big)/768 \\ = \;& T^{\Omega\cdot 2J}\cos(\pi\Omega\cdot X_2)\Big(5 + 15\cos^2(\pi\Omega\cdot X_1) + 3\cos^2(\pi\Omega\cdot X_2) \\ &+ \cos^2(\pi\Omega\cdot X_1)\cos^2(\pi\Omega\cdot X_2)\Big)/24 \end{aligned}$$

The second mid edge stencil is the same but rotated by 90° and its effect on the initial data is

$$\begin{aligned} &T^{\Omega\cdot 2J}\cos(\pi\Omega\cdot X_1)\Big(5 + 15\cos^2(\pi\Omega\cdot X_2) + 3\cos^2(\pi\Omega\cdot X_1) \\ &+ \cos^2(\pi\Omega\cdot X_2)\cos^2(\pi\Omega\cdot X_1)\Big)/24. \end{aligned}$$

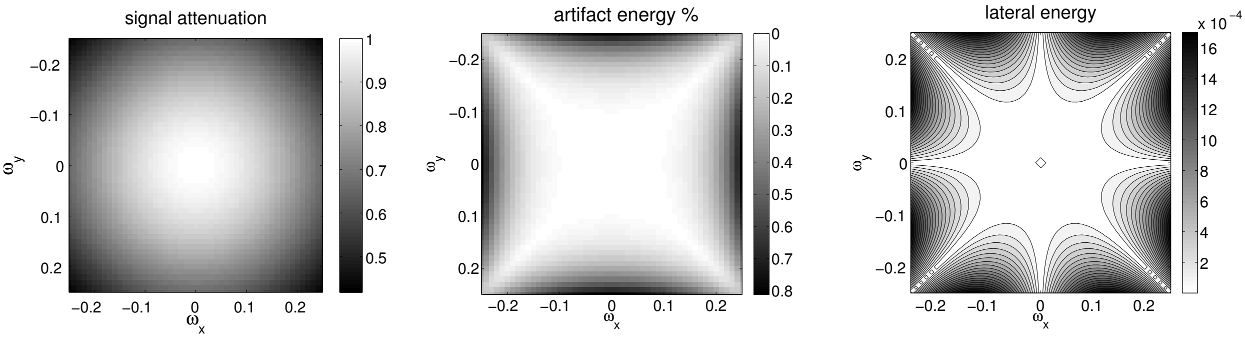

Figure 13: *Results for the 4-3 subdivision scheme in the limit as a function of sampling frequency. Left: the signal magnitude. Centre: the artifact energy as a percentage of the attenuated signal. Right: the lateral artifact.*

The mid face stencil is

$$\frac{1}{768}\begin{bmatrix} 0 & 8 & 8 & 0 \\ 8 & 176 & 176 & 8 \\ 8 & 176 & 176 & 8 \\ 0 & 8 & 8 & 0 \end{bmatrix} = \frac{1}{96}\begin{bmatrix} 0 & 1 & 1 & 0 \\ 1 & 22 & 22 & 1 \\ 1 & 22 & 22 & 1 \\ 0 & 1 & 1 & 0 \end{bmatrix}.$$

and its effect on the control data is

$$\begin{aligned}
&\Big(T^{\Omega\cdot 2(J-X_1/2-3X_2/2)} + T^{\Omega\cdot 2(J+X_1/2-3X_2/2)} + T^{\Omega\cdot 2(J-3X_1/2-X_2/2)} + 22T^{\Omega\cdot 2(J-X_1/2-X_2/2)} \\
&+22T^{\Omega\cdot 2(J+X_1/2-X_2/2)} + T^{\Omega\cdot 2(J+3X_1/2-X_2/2)} + T^{\Omega\cdot 2(J-3X_1/2+X_2/2)} + 22T^{\Omega\cdot 2(J-X_1/2+X_2/2)} \\
&+22T^{\Omega\cdot 2(J+X_1/2+X_2/2)} + T^{\Omega\cdot 2(J+3X_1/2+X_2/2)} + T^{\Omega\cdot 2(J-X_1/2+3X_2/2)} + T^{\Omega\cdot 2(J+X_1/2+3X_2/2)}\Big)/96 \\
= \;& T^{\Omega\cdot 2J}\Big(\cos(\pi\Omega\cdot X_1)\cos(\pi\Omega\cdot X_2)\Big(\cos^2(\pi\Omega\cdot X_1) + \cos^2(\pi\Omega\cdot X_2) + 4\Big)\Big)/6.
\end{aligned}$$

The limit points determined from the four limit stencils describe four different surfaces: $o\,T^{\Omega\cdot 2J}$, $p\,T^{\Omega\cdot 2J}$, $q\,T^{\Omega\cdot 2J}$ and $r\,T^{\Omega\cdot 2J}$, with

$$\begin{aligned}
o &= \Big((1+\cos^2(\pi\Omega\cdot X_1))(1+\cos^2(\pi\Omega\cdot X_2)) - 1\Big)/3 \\
r &= \cos(\pi\Omega\cdot X_1)\Big(5 + 15\cos^2(\pi\Omega\cdot X_2) + 3\cos^2(\pi\Omega\cdot X_1) + \cos^2(\pi\Omega\cdot X_2)\cos^2(\pi\Omega\cdot X_1)\Big)/24 \\
q &= \cos(\pi\Omega\cdot X_2)\Big(5 + 15\cos^2(\pi\Omega\cdot X_1) + 3\cos^2(\pi\Omega\cdot X_2) + \cos^2(\pi\Omega\cdot X_1)\cos^2(\pi\Omega\cdot X_2)\Big)/24 \\
p &= \Big(\cos(\pi\Omega\cdot X_1)\cos(\pi\Omega\cdot X_2)\Big(\cos^2(\pi\Omega\cdot X_1) + \cos^2(\pi\Omega\cdot X_2) + 4\Big)\Big)/6
\end{aligned}$$

The best sinusoidal approximation to the limit surface is given by $\alpha\,T^{\Omega\cdot 2J}$ and derived using equation (9) and leads to a signal magnitude, α, given by

$$\begin{aligned}
\alpha = \;& \cos^2(\pi\Omega\cdot X_1)\cos^2(\pi\Omega\cdot X_2) \\
&\times\Big(\cos^2(\pi\Omega\cdot X_1)\cos^2(\pi\Omega\cdot X_2) - \sin^2(\pi\Omega\cdot X_1)\sin^2(\pi\Omega\cdot X_2)\Big) \\
&\times\Big(\Big(1+\cos^2(\pi\Omega\cdot X_1)\Big)\Big(1+\cos^2(\pi\Omega\cdot X_2)\Big) - 1\Big)/3.
\end{aligned}$$

This is equivalent to what has been noted down in Table 6. Calculations for β, γ and δ are derived using equations (10), (11) and (12) respectively and yield the same results as shown in Table 6.

The most impressive improvements of the 4-3 box-spline scheme over the bicubic B-spline in terms of signal to artifact ratio in its surface is for features extrusions in a direction diagonal to the grid lines of the mesh.

We can already see from Table 5 that if extrusions run diagonal to the grid lines, the X_1 and X_2 artifact components are eliminated, because of the $\sin(\pi\Omega\cdot(X_1 \pm X_2)/2)$ terms in the expressions for the magnitude of the artifact components, which becomes zero if extrusion run diagonally. Therefore, adding a diagonal smoothing stage considerably reduces the total artifact found in diagonal extrusions. This confirms findings by Peters and Shiue (2004).

The reduction in artifact magnitude for extrusions diagonal to the grid lines is clearly visible in Figures 13 centre and right. However, we expect small artifacts to remain if extrusions run not entirely diagonal but at a smaller angle to the grid lines.

Next, we will see if we can improve upon this result by adding more smoothing operations in the diagonal direction.

7.4. The 4-8 box-spline

The 4-8 subdivision scheme generalises the four-directional box spline [Velho and Zorin (2001)]. It can be viewed as $\sqrt{2}$ scheme on quadrilateral meshes. Two steps of this subdivision scheme produce a binary scheme which can be examined using the analysis we applied to other binary schemes. Two $\sqrt{2}$ masks can be convolved to produce the mask of the binary scheme:

$$\frac{1}{64}\begin{bmatrix} 0 & 0 & 1 & 2 & 1 & 0 & 0 \\ 0 & 2 & 6 & 8 & 6 & 2 & 0 \\ 1 & 6 & 14 & 18 & 14 & 6 & 1 \\ 2 & 8 & 18 & 24 & 18 & 8 & 2 \\ 1 & 6 & 14 & 18 & 14 & 6 & 1 \\ 0 & 2 & 6 & 8 & 6 & 2 & 0 \\ 0 & 0 & 1 & 2 & 1 & 0 & 0 \end{bmatrix}. \tag{18}$$

Its z-transform is

$$4\left(\frac{1+z_1}{2}\right)^2\left(\frac{1+z_2}{2}\right)^2\left(\frac{1+z_1z_2}{2}\right)^2\left(\frac{1+z_2/z_1}{2}\right)^2 \quad \text{or} \tag{19}$$

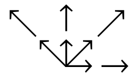

The magnitude of signal and artifact after two steps of 4-8 subdivision are shown in Table 7. To determine the amplification in the limit we have to apply the corresponding limit stencils.

The limit stencil for this scheme is given by:

$$\frac{1}{960}\begin{bmatrix} 0 & 1 & 6 & 1 & 0 \\ 1 & 44 & 118 & 44 & 1 \\ 6 & 118 & 280 & 118 & 6 \\ 1 & 44 & 118 & 44 & 1 \\ 0 & 1 & 6 & 1 & 0 \end{bmatrix}.$$

a	$c^2_{X_1} c^2_{X_2} c^2_{X_1+X_2} c^2_{X_1-X_2}$
b	$s^2_{X_1} c^2_{X_2} s^2_{X_1+X_2} s^2_{X_1-X_2}$
c	$c^2_{X_1} s^2_{X_2} s^2_{X_1+X_2} s^2_{X_1-X_2}$
d	$s^2_{X_1} s^2_{X_2} c^2_{X_1+X_2} c^2_{X_1-X_2}$

Table 7: *The signal and artifact magnitude after two 4-8 subdivision steps, where b, c and d are the X_1, X_2 and diagonal directions respectively.*

α	$c^2_{X_1} c^2_{X_2} c^2_{X_1+X_2} c^2_{X_1-X_2} \left(c^2_{X_1}(1 + c^2_{X_1}) + c^2_{X_2}(1 + c^2_{X_2}) + c^2_{X_1} c^2_{X_2}(c^2_{X_1} + c^2_{X_2} + 9)\right)/15$
β	$s^2_{X_1} c^2_{X_2} s^2_{X_1+X_2} s^2_{X_1-X_2} \left(s^2_{X_1}(1 + s^2_{X_1}) + c^2_{X_2}(1 + c^2_{X_2}) + s^2_{X_1} c^2_{X_2}(s^2_{X_1} + c^2_{X_2} + 9)\right)/15$
γ	$c^2_{X_1} s^2_{X_2} s^2_{X_1+X_2} s^2_{X_1-X_2} \left(c^2_{X_1}(1 + c^2_{X_1}) + s^2_{X_2}(1 + s^2_{X_2}) + c^2_{X_1} s^2_{X_2}(c^2_{X_1} + s^2_{X_2} + 9)\right)/15$
δ	$s^2_{X_1} s^2_{X_2} c^2_{X_1+X_2} c^2_{X_1-X_2} \left(s^2_{X_1}(1 + s^2_{X_1}) + s^2_{X_2}(1 + s^2_{X_2}) + s^2_{X_1} s^2_{X_2}(s^2_{X_1} + s^2_{X_2} + 9)\right)/15$

Table 8: *The signal and artifact magnitude in the limit surface when using the 4-8 box-spline scheme, where β, γ and δ are the X_1, X_2 and diagonal direction respectively.*

Its z-transform is

$$= \Bigg(\left(\frac{1+z_1}{2}\right)^2 \left(1 + \left(\frac{1+z_1}{2}\right)^2\right) + \left(\frac{1+z_2}{2}\right)^2 \left(1 + \left(\frac{1+z_2}{2}\right)^2\right)$$
$$+ \left(\frac{1+z_1}{2}\right)^2 \left(\frac{1+z_2}{2}\right)^2 \left(\left(\frac{1+z_1}{2}\right)^2 + \left(\frac{1+z_2}{2}\right)^2 + 9\right) \Bigg)/15.$$

The amplification terms for signal and artifact components resulting from this are listed in Table 8. The attenuation of the signal, the artifact energy as a percentage of the remaining signal and the lateral artifact energy are shown as a function of sampling frequency in Figure 14.

The same result could be obtained looking at the 4-8 limit surface directly. However, limit stencils for this scheme are very large and it is therefore easier to obtain signal and artifact magnitudes in the limit surface using the single step analysis method.

The improvement achieved by adding one more smoothing operation in the diagonal direction is significant. Comparing the results shown in Figure 14 to those plotted for the 4-3 scheme (Figure 13) we see that the improvement of the signal to artifact ratio is about a factor of 15, not only for extrusions in directions diagonal to the grid lines, but for all extrusions.

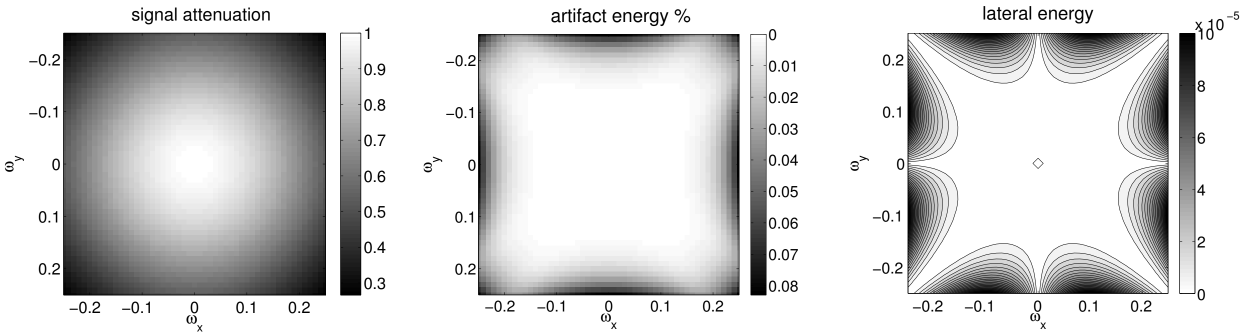

Figure 14: *Results for the 4-8 scheme in the limit as a function of sampling frequency. Left: the signal magnitude. Centre: the artifact energy as a percentage of the attenuated signal. Right: The corresponding lateral artifact magnitude.*

7.5. Kobbelt's interpolating box-spline

The Kobbelt (1996) scheme is an interpolatory tensor product scheme based on the univariate 4-point scheme (Dyn et al., 1987) and has the mask

$$\frac{1}{256}\begin{bmatrix} 1 & 0 & -9 & -16 & -9 & 0 & 1 \\ 0 & 0 & 0 & 0 & 0 & 0 & 0 \\ -9 & 0 & 81 & 144 & 81 & 0 & -9 \\ -16 & 0 & 144 & 256 & 144 & 0 & -16 \\ -9 & 0 & 81 & 144 & 81 & 0 & -9 \\ 0 & 0 & 0 & 0 & 0 & 0 & 0 \\ 1 & 0 & -9 & -16 & -9 & 0 & 1 \end{bmatrix} \tag{20}$$

The z-transform of this mask can be factorised into

$$\left(\frac{1+z_1}{2}\right)^4\left(\frac{1+z_2}{2}\right)^4\left(\frac{-1+4z_1-z_1^2}{2}\right)\left(\frac{-1+4z_2-z_2^2}{2}\right) \tag{21}$$

This scheme is not based on a box-spline. We have four smoothing stages in each of the gridline directions, like the bicubic B-spline discussed in Section 7.2, and a kernel.

The kernel, $\left(-1+4z_1-z_1^2\right)\left(-1+4z_2-z_2^2\right)/4$, can be expressed in terms of smoothing operators. We divide the kernel written in z-transform notation by a power of z so that the central value corresponds to z^0. This leads to

$$\left(\frac{-z_1^{-1}+4z_1^0-z_1}{2}\right)\left(\frac{-z_2^{-1}+4z_2^0-z_2}{2}\right) = \left(3-2\left(\frac{z_1^{-1}+2z_1^0+z_1^1}{4}\right)\right)\left(3-2\left(\frac{z_2^{-1}+2z_2^0+z_2^1}{4}\right)\right) \tag{22}$$

Because the scheme is interpolating the initial control points lie on the limit surface and the magnitudes of the signal and artifacts after one step, shown in Table 9, are the same as in the limit surface.

$a = \alpha$	$c^4_{X_1} c^4_{X_2}(3 - 2c^2_{X_1})(3 - 2c^2_{X_2})$
$b = \beta$	$s^4_{X_1} c^4_{X_2}(3 - 2s^2_{X_1})(3 - 2c^2_{X_2})$
$c = \gamma$	$c^4_{X_1} s^4_{X_2}(3 - 2c^2_{X_1})(3 - 2s^2_{X_2})$
$d = \delta$	$s^4_{X_1} s^4_{X_2}(3 - 2s^2_{X_1})(3 - 2s^2_{X_2})$

Table 9: *The magnitude of the signal term, α, and the artifact terms in the regular regions of Kobbelt's interpolating subdivision surface, where β, γ and δ are magnitudes of the X_1, X_2 and diagonal direction artifact components respectively. Because the subdivision scheme is interpolating the amplification terms after one step are the same as in the limit surface.*

The same results can be achieved when looking at the limit surface directly as demonstrated in examples discussed in Sections 7.1 – 7.3. For this scheme, however, it is easier to determine the amplitudes of the surface artifacts as shown here.

As can be clearly seen from Figure 15 the scheme retains the signal information better than the non-interpolating schemes discussed. But for interpolating schemes the artifact increases more than for non-interpolating schemes and as a result the artifact energy as a percentage of the remaining signal is large. The signal amplitude, the amplitude of the artifact energy as a percentage of the remaining signal and the amplitude of the lateral artifact are shown in Figure 15. All results are shown as a function of sampling frequency.

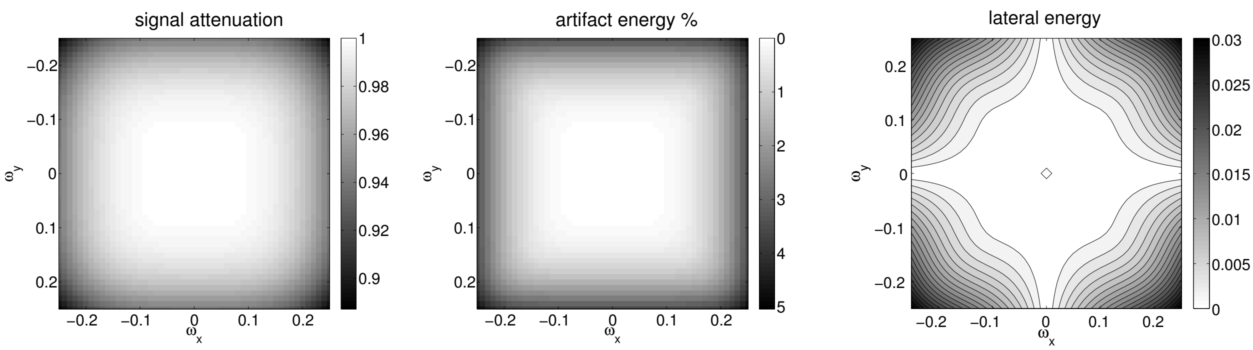

Figure 15: *Results for regular regions of Kobbelt's interpolating subdivision scheme in the limit shown as a function of sampling frequency. Left: the signal magnitude. Centre: the artifact energy as a percentage of the attenuated signal. Right: The lateral artifact.*

8. Summary

We have presented a uniform framework for analysing artifacts present in all surfaces which are specified in terms of quadrilateral control polyhedrons, i.e. NURBS, box-splines and regular subdivision surfaces. This complements our previous work on tuning the behaviour of subdivision around extraordinary vertices (Augsdörfer et al., 2006).

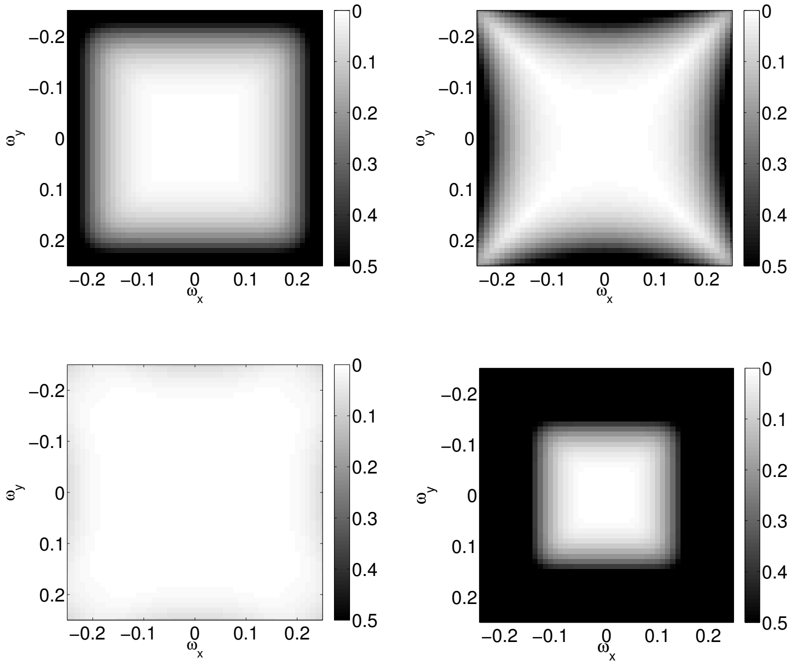

Figure 16: *Top row: The artifact energy as a percentage of the attenuated signal of bicubic B-spline (top left), 4-3 (top right), the 4-8 (bottom left) and Kobbelt's interpolating subdivision scheme (bottom right) in the limit as a function of sampling frequency. The result for all four schemes is shown on the same scale.*

We examined two mechanisms to analyse the magnitude of signal and artifact component in the limit surface: Firstly, by looking at the polyhedron after a single subdivision step in detail before establishing the limit artifact. Secondly, by examining the limit surface directly.

One subdivision step can be viewed as a two stage process involving a refinement or sampling stage followed by one or more smoothing stages. Artifact components are inevitably introduced in the sampling stage and the surface after sampling is made up of four components: one signal and three artifact components, one in the direction of each grid line and a third in the diagonal direction. All four surface components are attenuated in subsequent smoothing stages. Depending on the subdivision scheme smoothing stages involve different directions of smoothing. We show that if diagonal smoothing directions are involved the lateral artifact is significantly reduced. This is in accord with findings by Peters and Shiue (2004). This analysis also shows, for the first time, that schemes need to have smoothing factors along gridlines, because diagonal smoothing on its own will have the undesired effect to lead to large artifacts even for densely sampled control meshes. When handling schemes not based on box-splines we may encounter, alongside simple sampling and smoothing stages, a kernel from which no more smoothing stages can be extracted. By analysing the effect of the smoothing stages and the kernel on both the signal and the artifact components after sampling, we are able to make a statement about their magnitude after one subdivision step.

The magnitude of the signal and artifact component after one subdivision step will be reduced with further subdivision refinement steps. From the eigenstructure of the local subdivision matrix

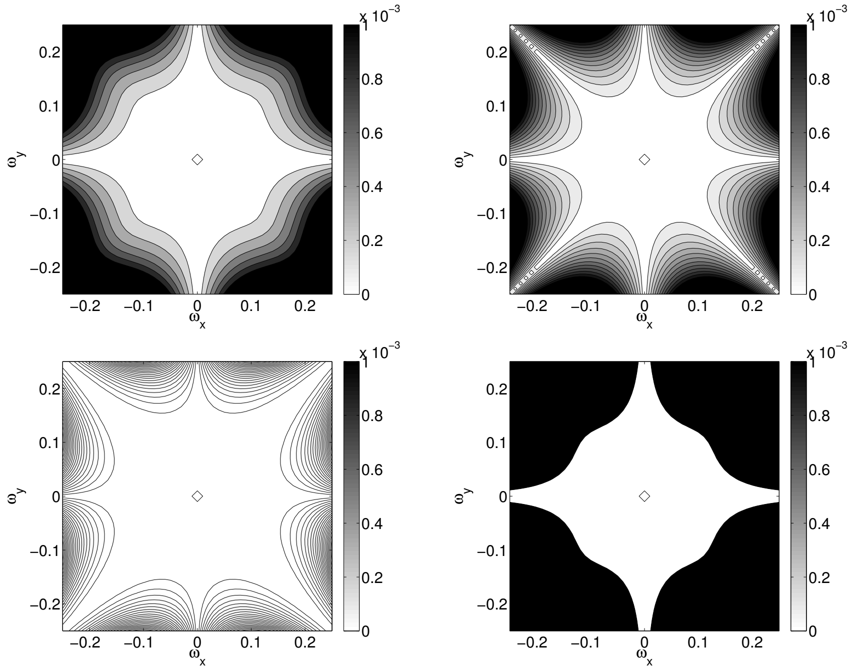

Figure 17: *Top row: The lateral artifact energy of the bicubic B-spline (top left), 4-3 (top right), the 4-8 (bottom left) and Kobbelt's interpolating subdivision scheme (bottom right) in the limit as a function of sampling frequency. The result for all four schemes is shown on the same scale.*

we can derive a limit stencil which enables us to derive points on the limit surface of a scheme. Again, by expressing the effect of a limit stencil in terms of mean smoothing and analysing its effect we can determine the magnitude of signal and artifact components in the limit surface.

By employing the limit stencil, for binary schemes, after one subdivision step we effectively look at vertex limit positions, mid face and mid edge limit positions of the input control mesh. Instead of examining a single subdivision step first, we may look at vertex, mid face and mid edge limit positions of the input control mesh directly by determining points on the limit surface using the limit stencil. To determine the respective limit stencils for binary schemes, or indeed any even scheme, we convolve the limit stencil with the mask of the scheme. For odd schemes, the respective stencil can be directly determined from the eigenstructure of the local subdivision matrix.

9. Conclusion

The analysis demonstrated here enables the designer to make a judgement on the necessary density of control points to use to be within certain required error margins. In the future, it may also help in the design of new box-spline algorithms, i.e. the analysis provides us with a tool to design schemes for which the error/artifact is zero at a certain sampling frequency.

Comparing results for the bilinear B-spline, the bicubic B-spline (regular regions of Catmull-Clark), the 4-3 box-spline, 4-8 box-spline and regular regions of Kobbelt's interpolating subdivision surface, shown in Figures 16, it is evident that, among these five schemes, the best behaviour in terms of artifact magnitude in the limit is given by the 4-8 scheme.

This analysis can be applied to the regular regions of any quadrilateral subdivision surface. Its extension to triangular schemes is not trivial and is the subject of other work (Augsdörfer et al., submitted to CAGD).

References

Augsdörfer, U., Dodgson, N., Sabin, M., 2006. Tuning subdivision by minimising gaussian curvature variation near extraordinary vertices. Computer Graphics Forum 25 (3), 263–272.

Augsdörfer, U., Dodgson, N., Sabin, M., submitted to CAGD. Artifact analysis on triangular box-splines surfaces.

Catmull, E., Clark, J., 1978. Recursively generated b-spline surfaces on arbitrary topological meshes. Computer Aided Design 10 (6), 183–188.

Dodgson, N., Augsdörfer, U., Cashman, T., Sabin, M., 2009. Deriving box-spline subdivision schemes. In: Maths of Surfaces XIII. p. to appear.

Dyn, N., 2002. Analysis of convergence and smoothness by the formalism of laurent polynomials. In: Iske, A., Quack, E., Floater, M. (Eds.), Tutorials on Multiresolution in Geometric Modelling. Springer, pp. 51–68.

Dyn, N., Levin, D., Gregory, J., 1987. A four-point interpolatory subdivision scheme for curve design. Computer Aided Geometric Design 4 (4), 257–268.

Halstead, M., Kass, M., DeRose, T., 1993. Efficient, fair interpolation using catmull-clark surfaces. In: Computer Graphics Proceedings, Annual Conference Series, 1993. ACM SIGGRAPH. pp. 35–44.

Kobbelt, L., 1996. Interpolatory subdivision on open quadrilateral nets with arbitrary topology. Computer Graphics Forum 15, 409–420.

Peters, J., Shiue, L.-J., 2004. Combining 4- and 3-direction subdivision. ACM Transactions on Graphics 23, 980–1003.

Sabin, M., 2002. Eigenanalysis and artifacts of subdivision curves and surfaces. In: Tutorials on Multiresolution in Geometric Modelling. Springer, pp. 69–92.

Sabin, M., Augsdörfer, U., Dodgson, N., 2005. Artifacts in box-spline surfaces. In: Mathematics of Surfaces XI. pp. 350–363.

Sabin, M., Barthe, L., 2003. Artifacts in recursive subdivision surfaces. In: Curve and Surface fitting: Saint-Malo 2002. Nashboro Press, Brentwood, TN, pp. 353–362.

Velho, L., Zorin, D., 2001. 4-8 subdivision. Computer Aided Geometric Design 18 (5), 397–427.